

1 **The new Kr-86 excess ice core proxy for synoptic activity: West Antarctic**
2 **storminess possibly linked to ITCZ movement through the last deglaciation**

3 Christo Buizert¹, Sarah Shackleton², Jeffrey P. Severinghaus², William H. G. Roberts³, Alan Seltzer^{2,4},
4 Bernhard Bereiter⁵, Kenji Kawamura⁶, Daniel Baggenstos⁵, Anaïs J. Orsi^{7,8}, Ikumi Oyabu⁶,
5 Benjamin Birner², Jacob D. Morgan², Edward J. Brook¹, David M. Etheridge^{9,10}, David Thornton^{9,10},
6 Nancy Bertler^{11,12}, Rebecca L. Pyne¹¹, Robert Mulvaney¹³, Ellen Mosley-Thompson¹⁴, Peter D. Neff^{15,16},
7 and Vasilii V. Petrenko¹⁶

8 ¹College of Earth, Ocean and Atmospheric Sciences, Oregon State University, Corvallis, OR 97331, USA

9 ²Scripps Institution of Oceanography, University of California San Diego, La Jolla, CA 92093, USA

10 ³Geography and Environmental Sciences, Northumbria University, Newcastle, UK and BRIDGE, School
11 of Geographical Sciences, University of Bristol, Bristol, UK

12 ⁴Marine Chemistry and Geochemistry Department, Woods Hole Oceanographic Institution, Woods Hole,
13 MA 02543, USA

14 ⁵Climate and Environmental Physics, Physics Institute, and Oeschger Center for Climate Research,
15 University of Bern, 3012, Bern, Switzerland

16 ⁶National Institute for Polar Research, 10-3 Midori-cho, Tachikawa, Tokyo 190-8518, Japan

17 ⁷Laboratoire des Sciences du Climat et de l'Environnement, LSCE/IPSL, CEA-CNRS-UVSQ, Université
18 Paris-Saclay, l'Orme des merisiers, Gif-sur-Yvette, France

19 ⁸Earth, Ocean and Atmospheric Sciences Department, The University of British Columbia, Vancouver, BC
20 V6T 1Z4, Canada

21 ⁹CSIRO Environment, PMB 1, Aspendale, Victoria 3195, Australia

22 ¹⁰Australian Antarctic Program Partnership, Institute for Marine & Antarctic Studies, University of
23 Tasmania, Hobart, Tasmania 7004, Australia

24 ¹¹Antarctic Research Centre, Victoria University of Wellington, Wellington, 6012, New Zealand

25 ¹²GNS Science, Lower Hut 5010, New Zealand

26 ¹³British Antarctic Survey, National Environment Research Council, Cambridge CB3 0ET, UK

27 ¹⁴Byrd Polar and Climate Research Center, The Ohio State University, Columbus, OH 43210, USA

28 ¹⁵Department of Soil, Water, and Climate, University of Minnesota, Saint Paul, MN 55108, USA

29 ¹⁶Department of Earth and Environmental Sciences, University of Rochester, Rochester, NY 14627, USA
30

31 *Correspondence to:* Christo Buizert (christo.buizert@oregonstate.edu)

32 **Abstract**

33 Here we present a newly developed ice core gas-phase proxy that directly samples a component of the
34 large-scale atmospheric circulation: synoptic-scale pressure variability. Surface pressure changes weakly
35 disrupt gravitational isotopic settling in the firn layer, which is recorded in krypton-86 excess ($^{86}\text{Kr}_{\text{xs}}$). The
36 $^{86}\text{Kr}_{\text{xs}}$ may therefore reflect the time-averaged synoptic pressure variability over several years (site
37 “storminess”), but it likely cannot record individual synoptic events as ice core gas samples typically
38 average over several years. We validate $^{86}\text{Kr}_{\text{xs}}$ using late Holocene ice samples from eleven Antarctic and
39 one Greenland ice core that collectively represent a wide range of surface pressure variability in the modern
40 climate. We find a strong spatial correlation ($r = -0.94, p < 0.01$) between site-average $^{86}\text{Kr}_{\text{xs}}$ and time-
41 averaged synoptic variability from reanalysis data. The main uncertainties in the analysis are the corrections
42 for gas loss and thermal fractionation, and the relatively large scatter in the data. Limited scientific
43 understanding of the firn physics and potential biases of $^{86}\text{Kr}_{\text{xs}}$ require caution in interpreting this proxy at
44 present. We show that Antarctic $^{86}\text{Kr}_{\text{xs}}$ appears to be linked to the position of the southern hemisphere eddy-
45 driven subpolar jet (SPJ), with a southern position enhancing pressure variability.

46 We present a $^{86}\text{Kr}_{\text{xs}}$ record covering the last 24 ka from the WAIS Divide ice core. Based on the empirical
47 spatial correlation of synoptic activity and $^{86}\text{Kr}_{\text{xs}}$ at various Antarctic sites, we interpret this record to show
48 that West Antarctic synoptic activity is slightly below modern levels during the last glacial maximum
49 (LGM); increases during the Heinrich Stadial 1 and Younger Dryas North Atlantic cold periods; weakens
50 abruptly at the Holocene onset; remains low during the early and mid-Holocene, and gradually increases to
51 its modern value. The WAIS Divide $^{86}\text{Kr}_{\text{xs}}$ record resembles records of monsoon intensity thought to reflect
52 changes in the meridional position of the intertropical convergence zone (ITCZ) on orbital and millennial
53 timescales, such that West Antarctic storminess is weaker when the ITCZ is displaced northward, and
54 stronger when it is displaced southward. We interpret variations in synoptic activity as reflecting movement
55 of the South Pacific SPJ in parallel to the ITCZ migrations, which is the expected zonal-mean response of
56 the eddy-driven jet in models and proxy data. Past changes to Pacific climate and the El Niño Southern
57 Oscillation (ENSO) may amplify the signal of the SPJ migration. Our interpretation is broadly consistent
58 with opal flux records from the Pacific Antarctic zone thought to reflect wind-driven upwelling.

59 We emphasize that $^{86}\text{Kr}_{\text{xs}}$ is a new proxy, and more work is called for to confirm, replicate and better
60 understand these results; until such time, our conclusions regarding past atmospheric dynamics remain
61 speculative. Current scientific understanding of firn air transport and trapping is insufficient to explain all
62 the observed variations in $^{86}\text{Kr}_{\text{xs}}$. A list of suggested future studies is provided.

63 **1 Introduction**

64 **1.1 Motivation and objectives**

65 Proxy records from around the globe show strong evidence for past changes in Earth's atmospheric
66 circulation and hydrological cycle that often far exceed those seen in the relatively short instrumental
67 period.

68 For example, low-latitude records of riverine discharge captured in ocean sediments (Peterson et al., 2000),
69 and isotopic composition of meteoric water captured in dripstone calcite (Cheng et al., 2016), suggest large
70 variations in tropical hydrology and monsoon strength, commonly interpreted as meridional migrations of
71 the intertropical convergence zone or ITCZ (Chiang and Friedman, 2012; Schneider et al., 2014). Such
72 ITCZ movement is seen both in response to insolation changes linked to planetary orbit (Cruz et al., 2005)
73 as well as in response to the abrupt millennial-scale Dansgaard-Oeschger (D-O) and Heinrich cycles of the
74 North-Atlantic (Kanner et al., 2012; Wang et al., 2001); the organizing principle is that the ITCZ follows
75 the thermal equator and therefore migrates towards the warmer (or warming) hemisphere (Broccoli et al.,
76 2006; Chiang and Bitz, 2005).

77 As a second example, the intensity of the El Niño – Southern Oscillation (ENSO), the dominant mode of
78 global interannual climate variability, has changed through time. A variety of proxy data suggest ENSO
79 activity in the 20th century was much stronger than in preceding centuries (Emile-Geay et al., 2015; Fowler
80 et al., 2012; Gergis and Fowler, 2009; Thompson et al., 2013). The vast majority of data and model studies
81 suggest weakened ENSO strength in the mid- and early-Holocene, likely in response to stronger orbitally-
82 driven NH summer insolation at that time (Braconnot et al., 2012; Cane, 2005; Clement et al., 2000; Driscoll
83 et al., 2014; Koutavas et al., 2006; Liu et al., 2000; Liu et al., 2014; Moy et al., 2002; Rein et al., 2005;
84 Tudhope et al., 2001; Zheng et al., 2008); yet other studies suggest there may not be such a clear trend, and
85 simply more variability (Cobb et al., 2013). Intensification of ENSO (or perhaps a more El-Niño-like mean
86 state) may have occurred during the North-Atlantic cold phases of the abrupt D-O and Heinrich cycles
87 (Braconnot et al., 2012; Merkel et al., 2010; Stott et al., 2002; Timmermann et al., 2007). Overall,
88 understanding past and future ENSO variability remains extremely challenging (Cai et al., 2015).

89 As a last example, the strength and meridional position of the southern hemisphere westerlies (SHW) is
90 thought to have changed in the past, which, via Southern Ocean wind-driven upwelling, has potential
91 implications for the global overturning circulation (Marshall and Speer, 2012) and for carbon storage in the
92 abyssal ocean (Anderson et al., 2009; Russell et al., 2006; Toggweiler et al., 2006). The SHW are thought
93 to be shifted equatorward (Kohfeld et al., 2013) during the last glacial maximum (LGM), a shift on which
94 climate models disagree (Rojas et al., 2009; Sime et al., 2013). During the abrupt D-O and Heinrich cycles,
95 the SHW move in parallel with the aforementioned migrations of the ITCZ in both data (Buizert et al.,
96 2018; Marino et al., 2013; Markle et al., 2017) and models (Lee et al., 2011; Pedro et al., 2018; Rind et al.,
97 2001).

98 As these examples clearly illustrate, evidence of past changes to the large-scale atmospheric circulation is
99 widespread. However, proxy evidence of such past changes is typically indirect – for example via isotopes
100 in precipitation, sea surface temperature, ocean frontal positions, windblown dust, or ocean upwelling –
101 complicating their interpretation. Here we present a newly developed noble gas-based ice core proxy, Kr-

102 $^{86}\text{Kr}_{\text{xs}}$), that directly samples a component of the large-scale atmospheric circulation: synoptic-
103 scale pressure variability. Owing to the firm air residence time of several years (Buizert et al., 2013) and the
104 gradual bubble trapping process, each ice core sample contains a distribution of gas ages, rather than a
105 single age. Therefore, $^{86}\text{Kr}_{\text{xs}}$ does not record the passing of individual weather systems, but rather the time-
106 average intensity of synoptic-scale barometric variability.

107 Here we provide the first complete description of this new proxy. We validate and calibrate $^{86}\text{Kr}_{\text{xs}}$ using
108 late-Holocene ice core samples from locations around Antarctica and Greenland that represent a wide range
109 of pressure variability in the modern climate. We discuss the difficulties in using this proxy (analytical
110 precision, surface melt, corrections for sample gas loss and thermal fractionation). Next, we use reanalysis
111 data to better understand the drivers of surface pressure variability in Antarctica. Last, we present an $^{86}\text{Kr}_{\text{xs}}$
112 records from the Antarctic WAIS Divide ice core through the last deglaciation.

113 1.2 Gravitational disequilibrium and Kr-86 excess

114 The upper 50-100 m of the ice sheet accumulation zone consists of firm, the unconsolidated intermediate
115 stage between snow and ice. An interconnected pore network exists within the firm, in which gas transport
116 is dominated by molecular diffusion (Schwander et al., 1993). Diffusion in this stagnant air column results
117 in gravitational enrichment in heavy gas isotopic ratios such as $\delta^{15/14}\text{N-N}_2$, $\delta^{40/36}\text{Ar}$ and $\delta^{86/82}\text{Kr}$ (Schwander,
118 1989; Sowers et al., 1992). In gravitational equilibrium, all these gases attain the same degree of isotopic
119 enrichment per unit mass difference:

$$120 \quad \delta_{\text{grav}}(z) = \left[\exp\left(\frac{\Delta m g z}{RT}\right) - 1 \right] \times 1000\text{‰} \quad (1)$$

121 with Δm the isotopic mass difference ($1 \times 10^{-3} \text{ kg mol}^{-1}$), g the gravitational acceleration, z the depth, R the
122 gas constant and T the temperature in Kelvin.

123 Besides molecular diffusion, firm air is mixed and transported via three other processes: downward
124 advection with the sinking ice matrix, convective mixing (used in the firm air literature as an umbrella term
125 to denote vigorous air exchange with the atmosphere via e.g. wind pumping and seasonal convection), and
126 dispersive mixing. These last three transport processes are all driven by large-scale air movement that does
127 not distinguish between isotopologues, and we refer to them collectively as macroscopic air movement. Of
128 particular interest for our proxy is dispersive mixing, which is driven by surface pressure variations. When
129 a low-pressure (high-pressure) system moves into the site, firm air at all depth levels is forced upwards
130 (downwards) to reach hydrostatic equilibrium with the atmosphere – a process called barometric pumping.
131 One can think of the firm layer “breathing” in and out in response to a rising and falling barometer,
132 respectively. Because firm has a finite dispersivity (Schwander et al., 1988), this air movement mixes the
133 interstitial firm air. Note that also an upward air movement exists in the firm column relative to the overall
134 downward advection of the ice, which is caused by the slow reduction of porosity with depth (Rommelaere
135 et al., 1997). This upward air flow due to gradual pore closure (around 10^{-9} to 10^{-8} m s^{-1}) is orders of
136 magnitude smaller than the flows driven via barometric pumping (around 10^{-6} m s^{-1}), and therefore
137 neglected here (Buizert and Severinghaus, 2016).

138 Any type of macroscopic air movement disturbs the gravitational settling, reducing isotopic enrichment
139 below δ_{grav} . Let $\delta^{86}\text{Kr}$, $\delta^{40}\text{Ar}$, and $\delta^{15}\text{N}$ refer to deviations of $^{86}\text{Kr}/^{82}\text{Kr}$, $^{40}\text{Ar}/^{36}\text{Ar}$, and $^{29}\text{N}_2/^{28}\text{N}_2$, respectively,

140 from their ratios in the well-mixed atmosphere. Gases that diffuse faster (such as N₂) will always be closer
 141 to gravitational equilibrium than gases that diffuse slower (such as Kr), and in the absence of thermal
 142 fractionation $\delta^{86}\text{Kr}/4 < \delta^{40}\text{Ar}/4 < \delta^{15}\text{N} < \delta_{\text{grav}}$. The isotopic differences $\delta^{86}\text{Kr}/4 - \delta^{40}\text{Ar}/4$ and $\delta^{86}\text{Kr}/4 - \delta^{15}\text{N}$
 143 thus reflect the degree of gravitational disequilibrium. The magnitudes of the isotopic disequilibria scale in
 144 a predictable way following the molecular diffusion coefficients (Birner et al., 2018); because the diffusion
 145 coefficients of N₂ and Ar are very similar, their disequilibria are comparable in magnitude. We define Kr-
 146 86 excess using the Kr and Ar isotopic difference:

$$147 \quad {}^{86}\text{Kr}_{\text{xs}40} = \frac{\delta^{86}\text{Kr}_{\text{corr}} - \delta^{40}\text{Ar}_{\text{corr}}}{\delta^{40}\text{Ar}_{\text{corr}}} \times 1000 \text{ per meg } \text{‰}^{-1} \quad (2)$$

148 where the “corr” subscript denotes a correction for gas loss (Appendix A1) and thermal fractionation
 149 (Appendix A2). The rationale for including a normalization in the denominator is discussed below. An
 150 alternative Kr-86 excess definition is possible using $\delta^{15}\text{N}$ instead of $\delta^{40}\text{Ar}$:

$$151 \quad {}^{86}\text{Kr}_{\text{xs}15} = \frac{\delta^{86}\text{Kr}_{\text{corr}}/4 - \delta^{15}\text{N}_{\text{corr}}}{\delta^{15}\text{N}_{\text{corr}}} \times 1000 \text{ per meg } \text{‰}^{-1} \quad (3)$$

152 Note that both definitions rely on having measurements of three isotope ratios ($\delta^{86}\text{Kr}$, $\delta^{40}\text{Ar}$ and $\delta^{15}\text{N}$), as
 153 the thermal correction requires $\delta^{40}\text{Ar}$ and $\delta^{15}\text{N}$ be known. The ${}^{86}\text{Kr}_{\text{xs}40}$ definition is preferred, because per
 154 unit mass difference $\delta^{40}\text{Ar}$ is less sensitive to thermal fractionation than $\delta^{15}\text{N}$ is (Grachev and Severinghaus,
 155 2003a; 2003b); this makes it more suitable for interpreting time series. Unless explicitly stated otherwise,
 156 we use ${}^{86}\text{Kr}_{\text{xs}40}$ as our definition of Kr-86 excess. The ${}^{86}\text{Kr}_{\text{xs}15}$ does provide a way to check the validity of
 157 ${}^{86}\text{Kr}_{\text{xs}40}$ timeseries, and indeed we find good correspondence between both definitions for the WDC
 158 deglacial timeseries. Because the disequilibrium signal is small, we express ${}^{86}\text{Kr}_{\text{xs}}$ in units of per meg (parts
 159 per million) of gravitational disequilibrium per ‰ of gravitational enrichment. This unit (per meg ‰⁻¹) is
 160 mathematically identical to ‰, but we use it to emphasize the normalization in the denominator.

161 In the (theoretical) case of full gravitational equilibrium (and no gas loss or thermal fractionation), $\delta^{86}\text{Kr}/4$
 162 $= \delta^{40}\text{Ar}/4 = \delta^{15}\text{N} = \delta_{\text{grav}}$, and therefore ${}^{86}\text{Kr}_{\text{xs}} = 0$. Any type of macroscopic mixing will cause $\delta^{86}\text{Kr}/4 <$
 163 $\delta^{40}\text{Ar}/4 < \delta^{15}\text{N} < \delta_{\text{grav}}$, and thus ${}^{86}\text{Kr}_{\text{xs}} < 0$. In this sense ${}^{86}\text{Kr}_{\text{xs}}$ is a quantitative measure for the degree of
 164 gravitational disequilibrium in the firn layer (Birner et al., 2018; Buizert and Severinghaus, 2016).

165 Kawamura et al. (2013) first describe this gravitational disequilibrium (or kinetic) fractionation effect at
 166 the Megadunes site (Severinghaus et al., 2010), where deep firn cracking leads to a 23 m-thick convective
 167 zone. They suggest that the isotopic disequilibrium can be used to estimate past convective zone thickness.
 168 We show here that sites with small convective zones can nevertheless have very negative ${}^{86}\text{Kr}_{\text{xs}}$, and instead
 169 we suggest that the ice core ${}^{86}\text{Kr}_{\text{xs}}$ is dominated by dispersive mixing driven by barometric pumping from
 170 time-averaged synoptic-scale pressure variability.

171 The principle behind ${}^{86}\text{Kr}_{\text{xs}}$ is illustrated with idealized firn model experiments in Fig. 1. In the absence of
 172 dispersive mixing (Fig. 1A, left panel), all isotope ratios approach δ_{grav} and $\delta^{86}\text{Kr} - \delta^{40}\text{Ar}$ is close to zero –
 173 but not exactly zero owing to downward air advection. Next, we replace a fraction f of the molecular
 174 diffusion with dispersive mixing. With dispersive mixing at $f = 0.1$ and $f = 0.2$ of total mixing (middle and

175 right panels, respectively), isotopic enrichment is progressively reduced below δ_{grav} (dashed line), making
176 $\delta^{86}\text{Kr} - \delta^{40}\text{Ar}$ (and consequently $^{86}\text{Kr}_{\text{xs}}$) increasingly negative.

177 The ratio of macroscopic over diffusive transport is expressed via the dimensionless Péclet number, given
178 here for advection and dispersion:

$$179 \quad \text{Pe}_X = \frac{w_{\text{air}}L + D_{\text{disp}}}{D_X} \quad (4)$$

180 where Pe_X is the Péclet number for gas X , w_{air} the (downward) advective air velocity, L a characteristic
181 length scale, D_X the diffusion coefficient for gas X , and D_{disp} is the dispersion coefficient (Buizert and
182 Severinghaus, 2016). In agreement with earlier studies (Birner et al., 2018; Kawamura et al., 2013), we find
183 that $\delta^{86}\text{Kr} - \delta^{40}\text{Ar}$ is maximized when molecular and dispersive mixing are equal in magnitude ($f = 0.5$, Fig.
184 1B), corresponding to $\text{Pe}_X \approx 1$. Note that $^{86}\text{Kr}_{\text{xs}}$ responds more linearly to f than $\delta^{86}\text{Kr} - \delta^{40}\text{Ar}$ does, due to
185 $\delta^{40}\text{Ar}$ in the denominator of Eq. (2).

186 In a last idealized experiment, we keep the fraction of dispersion fixed at $f = 0.1$ while we reduce the
187 thickness of the firn column by increasing the site temperature (Fig. 1C). We find that $\delta^{86}\text{Kr} - \delta^{40}\text{Ar}$ scales
188 linearly with firn thickness, here represented by $\delta^{40}\text{Ar}$ on the x-axis. However, $^{86}\text{Kr}_{\text{xs}}$ remains essentially
189 constant due to the normalization by $\delta^{40}\text{Ar}$ in the denominator of Eq. (2). The normalization step is thus
190 necessary to enable meaningful comparison between different sites and time periods that all have different
191 firn thicknesses. For this reason, the definition of $^{86}\text{Kr}_{\text{xs}}$ used here has been updated from the original
192 definition by (Buizert and Severinghaus, 2016).

193 Note that these highly idealized experiments assume dispersive mixing to be a fixed fraction of total
194 transport throughout the firn column, equivalent to a constant Péclet number in the diffusive zone (a
195 convective zone is absent in these simulations). In reality, the Péclet number varies greatly on all spatial
196 scales. On the macroscopic scale (> 1 m), Pe reflects the various transport regimes (Sowers et al., 1992),
197 being highest in the convective and lock-in zones. On the microscopic scale (< 1 cm), hydraulic
198 conductance scales as $\propto r^4$ (with r the pore radius) whereas the diffusive conductance scales as $\propto r^2$. This
199 means that the Darcy flow associated with barometric pumping will concentrate in the widest pores and
200 pathways, leading to a range of effective Péclet numbers within a single sample of firn. At intermediate
201 spatial scales of a few cm, firn density layering introduces strong heterogeneity in transport properties. It is
202 unclear at present whether the competition between diffusive and non-diffusive transport, which occurs at
203 the microscopic pore level, can be accurately represented in macroscopic firn air models via a linear
204 parameterization as is the current practice.

205

206 **2 Methods**

207 **2.1 Ice core sites**

208 In this study we use ice samples from eleven ice cores drilled in Antarctica, and one in Greenland. The
209 Antarctic sites are: West Antarctic Ice Sheet (WAIS) Divide core (WDC06A, or WDC), Siple Dome
210 (SDM), James Ross Island (JRI), Bruce Plateau (BRP), Law Dome DE08, Law Dome DE08-OH, Law
211 Dome DSSW20K, Roosevelt Island Climate Evolution (RICE), Dome Fuji (DF), EPICA (European Project
212 for Ice Coring in Antarctica) Dome C (EDC), and South Pole Ice Core (SPC14, or SP). Ice core locations
213 in Antarctica are shown in Fig. 2A. In Greenland, we use samples from the Greenland Ice Sheet Project 2
214 (GISP2).

215 We shall refer to late Holocene data from these sites as the calibration dataset, analogous to a core top data
216 set in the sediment coring literature. Site characteristics, coordinates, and number of samples included in
217 the calibration data set are given in Table 1. The DE08-OH site is a recent revisit of the Law Dome DE08
218 site. The DE08-OH core was measured at sub-annual resolution to understand cm-scale $^{86}\text{Kr}_{\text{xs}}$ variations
219 due to for example layering in firn density and bubble trapping (Appendix B). In addition to the calibration
220 data set, we present a record of Kr-86 excess going back to the LGM from WDC.

221 **2.2 Ice sample analysis**

222 We broadly follow analytical procedures described elsewhere (Bereiter et al., 2018a; Bereiter et al., 2018b;
223 Headly and Severinghaus, 2007; Severinghaus et al., 2003). In short, an 800 g ice sample, its edges trimmed
224 with a band saw to expose fresh surfaces, is placed in a chilled vacuum flask that is then evacuated for 20
225 minutes using a turbomolecular pump. Air is extracted from the ice by melting the sample while stirring
226 vigorously with a magnetic stir bar, led through a water trap, and cryogenically trapped in a dip tube
227 immersed in liquid He. Next, the sample is split into two unequal fractions. The smaller fraction (about 2%
228 of total air) is analyzed for $\delta^{15}\text{N-N}_2$, $\delta^{18}\text{O-O}_2$, $\delta\text{O}_2/\text{N}_2$ and $\delta\text{Ar}/\text{N}_2$ on a 3kV Thermo Finnigan Delta V plus
229 dual inlet IRMS (isotope ratio mass spectrometer). In the larger fraction, noble gases are isolated via hot
230 gettering to remove reactive gases. The purified noble gases are then analyzed for $\delta^{40/36}\text{Ar}$, $\delta^{40/38}\text{Ar}$, $\delta^{86/82}\text{Kr}$,
231 $\delta^{86/84}\text{Kr}$, $\delta^{86/83}\text{Kr}$, $\delta\text{Kr}/\text{Ar}$ and $\delta\text{Xe}/\text{Ar}$ on a 10kV Thermo Finnigan MAT253 dual inlet IRMS. We reject
232 one sample from RICE due to incomplete sample transfer, and one sample from WDC due to problems
233 with the water trap. Calibration is done for each measurement campaign by running samples of La Jolla
234 pier air.

235 All calibration (core top) data were measured using “Method 2” as described by Bereiter et al. (2018a),
236 with a longer equilibration time during the splitting step than used in that study to improve isotopic
237 equilibration between the fractions. The exception is the DE08-OH site, where the ice sample (rather than
238 the extracted gas sample) was split into two fractions – the advantage of this approach is that it does not
239 require a gas splitting step that is time-consuming and may fractionate the isotopes; the downside is that
240 the samples may have slightly different isotopic composition due to the stochastic nature of bubble trapping
241 and the different gas-loss histories of the ice pieces.

242 Measurements of the WDC downcore data set were performed over five separate measurement campaigns
243 that occurred in February-April 2014, February-April 2015, August 2015, August 2020, and August 2021,

244 respectively. The first three campaigns are described by Bereiter et al. (2018b), in which the $^{86}\text{Kr}_{\text{xs}}$ data are
245 a by-product of measuring $\delta\text{Kr}/\text{N}_2$ for reconstructing global mean ocean temperature. Campaigns 1 and 2
246 are in good agreement, whereas campaign 3 appears offset from the other two by an amount that exceeds
247 the analytical precision (offset around 35 per meg ‰^{-1}). To validate the main features in the record, we
248 performed two additional campaigns (4 and 5), in which all the gas extracted from each ice sample was
249 quantitatively gettered and only analysed for Ar and Kr isotopic composition. The downcore record, as well
250 as the five analytical campaigns, are discussed in detail in section 5.1. Data from the bubble-clathrate
251 transition zone (here 1000 to 1600 m depth, or $\sim 4\text{ka}$ to 7ka BP) are excluded owing to the potential for
252 artefacts; the depth range of the bubble-clathrate transition zone is based on observed positive anomalies in
253 $\delta\text{O}_2/\text{N}_2$ in WDC ice.

254 All samples were analyzed at Scripps Institution of Oceanography, USA, with the exception of the EDC
255 samples which were analyzed at University of Bern, Switzerland (Baggenstos et al., 2019). Some of the
256 EDC samples analyzed had clear evidence of drill liquid contamination, which acts to artefactually lower
257 $^{86}\text{Kr}_{\text{xs}}$ via isobaric interference on mass 82; the late Holocene data used here were not flagged for drill liquid
258 contamination (Baggenstos et al., 2019).

259 The 2σ analytical precision of the $\delta^{15}\text{N}$, $\delta^{40}\text{Ar}$, and $\delta^{86}\text{Kr}$ measurements is around 3, 5 and 26 per meg,
260 respectively, based on the reproducibility of La Jolla Air measurements. Via standard error propagation,
261 this results in a ~ 22 per meg ‰^{-1} (2σ) analytical uncertainty for both $^{86}\text{Kr}_{\text{xs}40}$ and $^{86}\text{Kr}_{\text{xs}15}$ at a site like WDC
262 where $\delta^{40}\text{Ar} \approx 1.2 \text{‰}$. We have no true (same-depth) replicates to assess the reproducibility of $^{86}\text{Kr}_{\text{xs}}$
263 measurements experimentally. The measured isotope ratios are corrected for gas loss (Δ_{GL}^{40}) and thermal
264 fractionation (Δ_{TF}^{86} , Δ_{TF}^{40} , Δ_{TF}^{15}) before interpretation; details on these corrections are given in appendix A.
265 For the coretop calibration study, the average magnitude of the gas loss and thermal fractionation
266 corrections is +14 and -15 per meg ‰^{-1} in $^{86}\text{Kr}_{\text{xs}}$, respectively. Note that these two corrections both involve
267 the $\delta^{40}\text{Ar}$ isotopic ratio, and therefore they are not independent from each other and not additive – in other
268 words, the total correction is not simply the sum of the two individual corrections.

269 Our study includes two ice cores from the Antarctic Peninsula: BRP (2 ice samples) and JRI (5 ice samples).
270 Measured $\delta\text{Xe}/\text{N}_2$ ratios (and to a lesser extent the $\delta\text{Kr}/\text{N}_2$ ratios) in all samples from both locations are
271 significantly elevated above the expected gravitational enrichment signal (Fig. A1A), which is clear
272 evidence for the presence of refrozen meltwater in these samples (Orsi et al., 2015). Like xenon, krypton is
273 highly soluble in (melt)water, and therefore $^{86}\text{Kr}_{\text{xs}}$ cannot be reliably measured in these samples; we reject
274 all samples from the BRP and JRI sites. It is notable that all samples from both sites show evidence of
275 refrozen meltwater, given that the high-accumulation BRP core is nearly entirely free of visible melt layers,
276 and that we carefully selected samples without visible melt features at JRI. Visible ice lenses form only
277 when meltwater pools and refreezes on top of low-permeability layers such as wind crusts; our observations
278 suggest meltwater can also refreeze throughout the firn in a way that cannot be detected visually.

279

280 3 Calibrating Kr-86 excess

281 The $^{86}\text{Kr}_{\text{xs}}$ proxy for synoptic activity was first proposed on theoretical grounds by Buizert and
282 Severinghaus (2016) – here we provide the first experimental validation of this proxy using a coretop
283 calibration of $^{86}\text{Kr}_{\text{xs}}$ using late-Holocene ice core samples from nine locations around Antarctica and one in
284 Greenland that represent a wide range of pressure variability in the modern climate (here: 1979-2017 CE).

285 3.1 Spatial variation in synoptic-scale pressure variability

286 Kr-86 excess is sensitive to air movement (both upward and downward), which in turn is controlled by the
287 magnitude of relative air pressure change. Let p_i be a time series of (synoptic-scale) site surface pressure
288 with N data points, time resolution Δt , and mean value \bar{p} . The time series can span a month, year, or multi-
289 year period, with \bar{p} potentially different for each month or year. We define the parameter Φ as:

$$290 \quad \Phi = \frac{1}{N\bar{p}} \sum_{i=1}^N \left| \frac{p_i - p_{i-1}}{\Delta t} \right| \quad (5)$$

291 which we here express in convenient units of $\% \text{ day}^{-1}$. Φ reflects the intensity of barometric pumping in the
292 firn column. Note that Δt should be larger than ~ 1 hour, which is the timescale for the entire firn column to
293 equilibrate with the surface pressure (Buizert and Severinghaus, 2016), and smaller than about a day in
294 order to adequately resolve synoptic-scale pressure events. Here we use ERA-interim reanalysis data from
295 1979-2017 with $\Delta t = 6$ hours (Dee et al., 2011), from which we calculate monthly and annual Φ values
296 using Eq. (5). A map of annual-mean Φ across Antarctica is given in Fig. 2A. At all sites considered, Φ has
297 a strong seasonal cycle with pressure variability/storminess being strongest in the local winter season (Fig.
298 2C). Interannual differences in Φ are greatest along the Siple coast and coastal West Antarctica (Fig. 2B),
299 mainly reflecting the influence of central Pacific (ENSO, PDO) climate variability (Section 4).

300 3.2 Kr-86 excess proxy calibration

301 Present-day Antarctica has a wide range of Φ (Fig. 2A), which allows us to validate and calibrate $^{86}\text{Kr}_{\text{xs}}$. In
302 Fig. 3A we plot the site mean $^{86}\text{Kr}_{\text{xs}40}$ (with $\pm 1\sigma$ error bars) as a function of Φ (averaged over full 1979-
303 2017 period). We find a Pearson correlation coefficient of $r = -0.94$ when using site mean $^{86}\text{Kr}_{\text{xs}40}$, and $r =$
304 -0.83 when using the $^{86}\text{Kr}_{\text{xs}40}$ of individual samples, respectively ($p < 0.01$). Note that in this particular case
305 the site-mean $^{86}\text{Kr}_{\text{xs}40}$ and $^{86}\text{Kr}_{\text{xs}15}$ are identical (because by design, after thermal correction $\delta^{15}\text{N} = \delta^{40}\text{Ar}$);
306 the error bars are different, though.

307 The $^{86}\text{Kr}_{\text{xs}}$ data have been corrected for gas loss (Appendix A1) and thermal fractionation (Appendix A2);
308 with the gas loss correction being the more uncertain component. Figure 3B shows the correlations of the
309 calibration curve as a function of the gas loss scaling parameter ϵ_{40} . We find a good correlation over a wide
310 range of ϵ_{40} values, proving our calibration is not dependent on the choice of ϵ_{40} . When using uncorrected
311 $^{86}\text{Kr}_{\text{xs}40}$ data the site mean correlation is $r = -0.71$; when applied individually, both the gas loss and thermal
312 correction each improve the correlation to $r = -0.77$ and $r = -0.79$, respectively (Fig. A3, all $p < 0.05$). Based
313 on these tests we conclude that the observed relationship is not an artefact of the applied corrections. The
314 applied corrections improve the correlation, which increases confidence in the method. The calibration
315 results for $^{86}\text{Kr}_{\text{xs}15}$ are shown in Fig. A4.

316 Notably, there is a large spread in $^{86}\text{Kr}_{\text{xs}}$ across samples from any single site, particularly at the high- Φ sites
317 of SDM and RICE (Fig. 3A, note the $\pm 1\sigma$ error bars). This spread is larger than the measurement
318 uncertainty, and we believe this variance reflects a signal that is truly present in the ice. The Siple coast and
319 Roosevelt Island experience the largest Φ interannual differences in Antarctica (Fig. 2B), and it is therefore
320 likely that our coarse sampling is aliasing the true $^{86}\text{Kr}_{\text{xs}}$ signal. The variance in $^{86}\text{Kr}_{\text{xs}}$ may contain climate
321 information also.

322 Both theoretical considerations and observations thus suggest $^{86}\text{Kr}_{\text{xs}}$ is a proxy for time-averaged barometric
323 surface pressure variability at the site, and in the remainder of this manuscript we will interpret it as such.

324 3.3 Discussion of the Kr-86 excess proxy

325 Our interpretation of $^{86}\text{Kr}_{\text{xs}}$ as a proxy for time-averaged pressure variability is somewhat complicated by
326 the possibility of deep convective zones, which have the same $^{86}\text{Kr}_{\text{xs}}$ signature as barometric pumping. This
327 was discovered at the Megadunes (MD) site, central East Antarctica; at this zero-accumulation site deep
328 cracks form in the firn layer that facilitate a 23 m deep convection zone (Severinghaus et al., 2010). In fact,
329 this observation led earlier work to suggest that noble gas gravitational disequilibrium may be used as a
330 proxy for convective zone thickness (Kawamura et al., 2013), rather than synoptic-scale pressure variability
331 as suggested here. Although megadunes and zero-accumulation zones are ubiquitous and cover 20% of the
332 Antarctic Plateau (Fahnestock et al., 2000), ice cores are seldom drilled in these areas and it is safe to
333 assume that they never formed at sites like WAIS Divide that had relatively high accumulation rates even
334 during the last glacial period. Performing the corrections for thermal and size-dependent fractionation is
335 challenging at MD, and we suggest that the MD $^{86}\text{Kr}_{\text{xs}}$ is in the range of -2 to -55 per meg ‰^{-1} ; even at the
336 larger limit, this is still smaller in magnitude than $^{86}\text{Kr}_{\text{xs}}$ anomalies at several modern-day sites with small
337 convective zones (such as SDM, RICE and the Law Dome sites), suggesting barometric pumping is capable
338 of producing larger $^{86}\text{Kr}_{\text{xs}}$ signals than even the most extreme observed case of convective surface mixing.
339 Having $^{86}\text{Kr}_{\text{xs}}$ measured in MD ice core (rather than firn air) samples would be valuable for a more
340 meaningful comparison to the ice core sample measurements presented here. Windy sites can have
341 substantial convective zones of ~ 14 m (Kawamura et al., 2006), and future studies of $^{86}\text{Kr}_{\text{xs}}$ at such sites
342 would be valuable.

343 Currently, 1-D and 2-D firn air transport model simulations underestimate the magnitude of the $^{86}\text{Kr}_{\text{xs}}$ signal
344 compared to measurements in mature ice samples (Birner et al., 2018), complicating scientific
345 understanding of the proxy. In these models, the effective molecular diffusivity of each gas is scaled linearly
346 to its free air diffusivity. The ratio of krypton to argon free air diffusivity is 0.78. This ratio, which directly
347 sets the magnitude of the simulated $^{86}\text{Kr}_{\text{xs}}$, may actually be smaller than 0.78 in real firn, as krypton is more
348 readily adsorbed onto firn surfaces retarding its movement (similar to gasses moving through a gas
349 chromatography column). This may be one explanation for why models simulate too little $^{86}\text{Kr}_{\text{xs}}$.

350 Another likely explanation for the model-data mismatch is that certain critical sub-grid processes (such as
351 the aforementioned pore-size dependence of the Péclet number) are not adequately represented in these
352 models. Barometric pumping may further actively shape the pore network through the movement of water
353 vapor, thereby keeping certain preferred pathways connected and open below the density where percolation
354 theory would predict their closure (Schaller et al., 2017). The fate of a pore restriction is determined by the
355 balance between the hydrostatic pressure (that acts to close it) and vapor movement away from its convex

356 surfaces (that acts to keep it open); we speculate that barometric Darcy air flow keeps high-flow channels
357 connected longer by eroding convex surfaces. This enhances the complexity (and therefore dispersivity) of
358 the deep firn pore network and possibly creates a non-linear $^{86}\text{Kr}_{\text{xs}}$ response to barometric pumping. The
359 hypothesized channel formation in deep firn is driven by a positive feedback on flow volume, and somewhat
360 reminiscent of erosion-driven stream network formation in fluvial geomorphology.

361 Firn models predict that, after correcting for thermal fractionation, the deviation from gravitational
362 equilibrium for the elemental ratios (such as $\delta\text{Kr}/\text{Ar}$) should be proportional to that deviation in isotopic
363 ratios. However, the observations suggest that the former is usually smaller than would be expected from
364 the latter. As before, adsorption of Kr onto firn grain surfaces may contribute to the observed discrepancy,
365 and laboratory tests of this process are called for. Further, the impacts of gas loss are greater on elemental
366 ratios than on the isotopic ratios which may contribute also. Including measurements of xenon isotopes and
367 elemental ratios in future measurement campaigns may be able to provide additional constraints to better
368 understand this discrepancy.

369 Measurements on firn air samples, where available, suggest a smaller $^{86}\text{Kr}_{\text{xs}}$ anomaly in firn air than found
370 in ice core samples from the same site. We attribute this in part to a seasonal bias that is introduced by the
371 fact that firn air sampling always takes place during the summer months, whereas the synoptic variability
372 that drives the Kr-86 excess anomalies is largest during the winter (Fig. 2C); consequently, firn air
373 observations are biased towards weaker $^{86}\text{Kr}_{\text{xs}}$. Further, in the deep firn where $^{86}\text{Kr}_{\text{xs}}$ anomalies are largest,
374 firn air pumping may not yield a representative air sample, but rather be biased towards the well-connected
375 porosity at the expense of poorly-connected cul-de-sac-like pore clusters. Since barometric pumping
376 ventilates this well-connected porespace with low- $^{86}\text{Kr}_{\text{xs}}$ air from shallower depths, the firn air sampling
377 may not capture a representative $^{86}\text{Kr}_{\text{xs}}$ value of the full firn air content. These explanations are all somewhat
378 speculative, and a definitive understanding of the firn-ice differences is lacking at this stage.

379 Gas loss and thermal corrections are critical to the interpretation of $^{86}\text{Kr}_{\text{xs}}$. The thermal correction is applied
380 to account for thermal gradients in the firn (ΔT , here defined as the temperature at the top minus the
381 temperature at the base of the firn), which are chiefly caused by geothermal heat or surface temperature
382 changes at the site. At low-accumulation sites geothermal heating leads to $\Delta T < 0$. We use ^{15}N -excess ($\delta^{15}\text{N}$
383 $- \delta^{40}\text{Ar}/4$) to estimate the thermal gradient in the firn (Appendix A2). Because nitrogen and argon have
384 similar diffusivities but different thermal diffusion coefficients, $\delta^{15}\text{N} - \delta^{40}\text{Ar}$ is relatively insensitive to
385 barometric pumping yet sensitive to thermal fractionation, allowing estimating ΔT .

386 Besides the actual thermal gradients in the firn, the isotopic composition may also be impacted by seasonal
387 rectifier effects. If the firn air transport properties differ between the seasons (for example due to thermal
388 contraction cracks, convective instabilities, or seasonality in wind pumping), this can result in a thermal
389 fractionation of isotopic ratios in the absence of a thermal gradient ΔT in mean annual temperature (Morgan
390 et al., 2022).

391 For the WDC, DSS and GISP2 sites we obtain ΔT values close to zero as expected for these high-
392 accumulation sites; for the SP, SDM, RICE, and DF sites we find ΔT ranging from -0.76 to -1.18°C, in
393 agreement with the effect of geothermal heat. The high-accumulation DE08 and DE08-OH sites both have
394 an unexpectedly large ΔT of -1.6°C; the good agreement between the sites suggest it is likely a real signal,

395 yet we can rule out geothermal heat as the cause. This may suggest that the Law Dome DE08 site is subject
396 to a seasonal rectifier effect, or a recent climatic cooling. Last, the EDC site shows an unexpected positive
397 $\Delta T = +1.6 \pm 1.89^\circ\text{C}$. Three possible explanations are: (1) the aforementioned drill liquid contamination for
398 this core (Baggenstos et al., 2019); (2) a summertime-biased seasonal rectifier; or (3) an over-correction of
399 $\delta^{40}\text{Ar}$ for gas loss, which could occur for example if natural and post-coring fugitive gas loss fractionate
400 $\delta^{40}\text{Ar}$ differently and EDC samples were impacted mostly by the former type (our correction is mostly
401 based on measurements of the latter type).

402 For the Law Dome DE08-OH site we observe large (5-fold) sub-annual variations in $^{86}\text{Kr}_{\text{xs}}$ (Fig. B1). The
403 magnitude of the $^{86}\text{Kr}_{\text{xs}}$ layering is truly remarkable. The isotopic enrichment of each gas ($\delta^{15}\text{N}$, $\delta^{40}\text{Ar}$,
404 $\delta^{86}\text{Kr}$) can be converted to an effective diffusive column height (DCH). For the samples with the smallest
405 (greatest) $^{86}\text{Kr}_{\text{xs}}$ magnitude, this DCH is around 1 m (6 m) shorter for $\delta^{86}\text{Kr}$ than it is for $\delta^{15}\text{N}$. The firm air
406 transport physics that may explain such phenomena are beyond our current scientific understanding. The
407 sub-annual variations may be related to the seasonal cycle in storminess, though that seems improbable to
408 us at present as the gas age distribution at the depth of bubble closure has a width of several years
409 (Schwander et al., 1993). Another reason may be seasonal layering in firm properties – such as density,
410 grain size, and pore connectivity – that control the degree of disorder and dispersive mixing occurring in
411 the firm, and lead to a staggered firm trapping and seasonal variations in Δage (Etheridge et al., 1992; Rhodes
412 et al., 2016). The sample air content estimated from the IRMS inlet pressure is similar for all measurements,
413 making it unlikely that the variations in $^{86}\text{Kr}_{\text{xs}}$ are caused by remnant open porosity in lower-density layers.
414 In any case it is remarkable that such large variations in gas composition can arise and persist on such small
415 length scales, given the relatively large diffusive, dispersive, and advective transport length scales of the
416 system. More work is needed to establish the origin of the sub-annual variations in ice core $^{86}\text{Kr}_{\text{xs}}$. At all
417 other sites analyzed here, the sample length exceeds the annual layer thickness; this will remove some, but
418 not all, of the effects of the sub-annual variations.

419 Another puzzling observation is the positive $^{86}\text{Kr}_{\text{xs}}$ at the Dome Fuji (DF) site; theoretical considerations
420 suggest it should always be negative. In part this may be due to an over-correction of $\delta^{40}\text{Ar}$ for gas loss,
421 which would act to bias $^{86}\text{Kr}_{\text{xs}}$ in the positive direction. This correction is largest at DF owing to the very
422 negative $\delta\text{O}_2/\text{N}_2$ and $\delta\text{Ar}/\text{N}_2$ (Fig. A1); while we base our correction on published work, it is conceivable
423 that we overestimate the true correction (Appendix A1). In particular, our gas loss correction is based on
424 observations on artefactual post-coring gas loss, which may fractionate $\delta^{40}\text{Ar}$ differently than natural
425 fugitive gas loss during bubble close-off. Omitting the gas loss correction indeed makes $^{86}\text{Kr}_{\text{xs}}$ at DF
426 negative (Fig. A3C-D). Another hypothesis is that the positive $^{86}\text{Kr}_{\text{xs}}$ signal is an artefact of the seasonal
427 rectifier that Morgan et al. (2022) identify at DF. In this work we assume a linear approach in which the
428 effect of the rectifier can be described by a single ΔT value that is the same for isotopic pairs. In reality,
429 there may be non-linear interactions between thermal fractionation and firm advection that impact the
430 isotopic values of the various gases in a more complex way than captured in our approach.

431 The $^{86}\text{Kr}_{\text{xs}}$ is also correlated with other site characteristics besides Φ . For site elevation we find $r = 0.96$
432 (0.84); and for mean annual temperature $r = -0.87$ (-0.76); the number in parentheses gives the correlation
433 when using all the individual samples rather than site-mean $^{86}\text{Kr}_{\text{xs}}$. The listed correlations all have $p < 0.01$.
434 For site accumulation we do not find a statistically significant correlation at the 90% confidence level. The
435 correlations with elevation and temperature are comparable to those we find for Φ ; this is no surprise given

436 that elevation, Φ and T are all strongly correlated with one another, mainly because elevation directly
437 impacts both T (via the lapse rate) and Φ (via its topographic influence on the position of storm tracks). To
438 our knowledge there are no mechanisms through which either elevation or annual-mean temperature could
439 drive kinetic isotopic fractionation in the firn layer. Perhaps other unexamined site characteristics (such as
440 the degree of density layering, or the magnitude of the annual temperature cycle) could provide good
441 correlations also, suggesting additional hidden controls on $^{86}\text{Kr}_{\text{xs}}$. The data needed to assess such hidden
442 controls are not available for most sites.

443 The calibration of the $^{86}\text{Kr}_{\text{xs}}$ proxy is based on spatial regression. In applying the proxy relationship to
444 temporal records, we make the implicit assumption that proxy behavior in the temporal and spatial
445 dimensions is at least qualitatively similar. This assumption may prove incorrect. In particular, changes in
446 insolation are known to impact firn microstructure and bubble close-off characteristics, which in turn
447 impacts gas records of $\delta\text{O}_2/\text{N}_2$ and total air content (Bender, 2002; Raynaud et al., 2007). Since $^{86}\text{Kr}_{\text{xs}}$ is
448 linked to the dispersivity of deep firn, it seems probable that insolation has a direct impact on $^{86}\text{Kr}_{\text{xs}}$ also via
449 the firn microstructure. We will revisit this issue in our interpretation of the WDC $^{86}\text{Kr}_{\text{xs}}$ record (Section 5).
450 Overall, we anticipate $^{86}\text{Kr}_{\text{xs}}$ to be a qualitative proxy for synoptic variability, yet want to caution against
451 quantitative interpretation based on the spatial regression slope.

452 The observations presented in this section clearly highlight the fundamental shortcomings of our current
453 understanding of firn air transport hinting at the existence of complex interactions, presumably at the pore-
454 scale, that are not being represented. Percolation theory finds that near the critical point (presumably the
455 lock-in depth) a network becomes fractal in its nature; we suggest that this fractal nature of the pore network
456 likely contributes to non-linear pore-scale interactions that give rise to the $^{86}\text{Kr}_{\text{xs}}$ observations in ice. While
457 the observed correlation of Fig. 3A is highly encouraging, further work is critical to understand this proxy.
458 Examples of such future studies are: (1) additional high-resolution records that can resolve the true
459 variations that exist in a single ice core, similar to the DE08-OH record; (2) 3-D firn air transport model
460 studies; (3) improvements to the gas loss correction; (4) additional coring sites to extend the spatial
461 calibration and further confirm the validity of the proxy; (5) Adding xenon isotopic constraints (^{136}Xe
462 excess) as an additional marker of isotopic disequilibrium; (6) numerical simulations of pore-scale air
463 transport in large-scale firn networks; (7) experimental studies of dispersion and noble gas adsorption in
464 firn samples; (8) percolation theory approaches to study the fractal nature of the pore network of the lock-
465 in zone; and (9) replication of the WDC deglacial $^{86}\text{Kr}_{\text{xs}}$ record in nearby ice cores such as RICE.

466 **4 Present-day controls on Kr-86 excess in Antarctica**

467 In this section we investigate the large-scale patterns of climate variability in the Southern Hemisphere that
468 could affect Φ and therefore $^{86}\text{Kr}_{\text{xs}}$ over Antarctica. We begin by investigating the patterns in the wind field
469 that are associated with changes in Φ at ice core sites, before examining how more canonical patterns of
470 Southern Hemisphere climate variability, such as the southern annular mode (SAM), might affect Φ over
471 the whole of Antarctica.

472 We use ERA-interim reanalysis data for the 1979-2017 period (Dee et al., 2011) to evaluate the present-
473 day controls on synoptic-scale pressure variability in Antarctica. Kr-86 excess in an ice core sample
474 averages over several years of pressure variability, and therefore we focus on annual-mean correlation in
475 our analysis. The annual-mean Φ is calculated from the 6-hourly reanalysis data using Eq. (5). Note that
476 we let the year run from April to March to avoid dividing single El Niño / La Niña events across multiple
477 years.

478 At all Antarctic sites investigated, a similar pattern exists; four representative locations are shown in Fig.
479 4, where we regress the zonal wind in the lower (850 hPa, color shading) and upper troposphere (200 hPa,
480 contours) onto our surface pressure variability parameter Φ . We find that synoptic pressure variability at
481 these sites is linked to zonal winds along the southern margin of the eddy-driven subpolar jet (SPJ), which
482 extends from the surface to the upper troposphere (Nakamura and Shimpo, 2004; Trenberth, 1991). Sites
483 near the ice sheet margin (Figs. 4A, B and D) are most sensitive to the SPJ edge in their sector of Antarctica,
484 whereas interior sites (Fig. 4C) appear sensitive to the overall strength/position of the SPJ. Note that
485 strengthening, broadening or southward shifting of the SPJ all can in principle enhance site Φ .

486 Pressure variability at WDC is furthermore correlated with the strength of the Pacific Subtropical jet (STJ)
487 aloft (solid contour lines centered around 30°S in the Pacific in panel 4A), forming an upper troposphere
488 wind pattern that resembles the wintertime South Pacific split jet (Bals-Elsholz et al., 2001; Nakamura and
489 Shimpo, 2004); this agrees with the finding that a strengthening of the split jet enhances storminess over
490 West Antarctica (Chiang et al., 2014).

491 Next, we investigate how the well-known patterns of large-scale atmospheric variability, such as SAM and
492 ENSO, impact pressure variability in Antarctica. Figure 5 shows the correlation of Φ with the three leading
493 modes of SH extra-tropical atmospheric variability; the correlation with various indices and modes for
494 individual ice core locations is given in Table 2. Most teleconnection patterns have a specific season during
495 which they are strongest; here we do not differentiate between seasons, because $^{86}\text{Kr}_{\text{xs}}$ in ice core samples
496 averages over all seasons.

497 Globally, annual-mean Φ is highest over the Southern Ocean (Fig. 5A); a region of enhanced baroclinicity
498 associated with the eddy-driven SPJ (Nakamura and Shimpo, 2004). The green line denotes the latitude of
499 maximum Φ , corresponding roughly to the latitude with the highest storm track density (57.8°S on average).

500 The dominant mode of atmospheric variability in the SH extratropics is the southern annular mode,
501 representing the vacillation of atmospheric mass between the mid- and high-latitudes (Thompson and
502 Wallace, 2000). Figure 5B shows 500 hPa geopotential height (Z500) anomalies associated with the SAM
503 as contours, with the color shading giving the correlation between Φ and the SAM index. During the

504 positive SAM phase (negative Z500 over Antarctica) we find that the stormtracks and maximum synoptic
505 activity are displaced towards Antarctica (positive Φ correlation poleward of the green line in Fig. 5B).
506 This is associated with a strengthening and poleward displacement of the SH westerly winds that occurs
507 during a positive SAM phase. More locally, Φ on the Antarctic Peninsula is positively correlated with the
508 SAM-index (Table 2); Φ at the other sites is not meaningfully impacted. This suggests that the variations
509 associated with the SAM (as commonly defined) do not extend far enough poleward to meaningfully impact
510 Antarctica with the exception of the Peninsula. Enhanced synoptic variability on the Peninsula during
511 positive SAM phases is consistent with observations of enhanced snowfall at those times (Thomas et al.,
512 2008).

513 The second mode of SH extratropical variability is the Pacific-South American Mode 1 (PSA1), which
514 reflects a Rossby wave response to sea surface temperature (SST) anomalies over the central and eastern
515 equatorial Pacific (Mo and Paegle, 2001), and is therefore closely linked to ENSO on interannual time
516 scales (we find a correlation of $r = 0.77$ between the annual mean PSA1 and Niño 3.4 indices). Φ in the
517 Amundsen and Ross Sea sectors (WDC, SDM and RICE) is positively correlated to the PSA1 and Niño 3.4
518 SST, suggesting larger synoptic activity during El Niño phases and low activity during La Niña phases. The
519 PSA2 pattern, also linked to SST anomalies in the tropical Pacific (Mo and Paegle, 2001), is likewise
520 correlated to Φ in the Amundsen and Ross Sea sectors (Fig. 5C and Table 2). While all the correlations
521 listed are statistically significant, they explain only a fraction of the total variability.

522 Next, we consider anomalies in sea ice area and extent (Parkinson and Cavalieri, 2012). We focus on the
523 Ross and Amundsen-Bellingshausen Seas where impacts on WAIS Divide may be expected. At the 90%
524 confidence level we do not find significant correlations to sea ice area or extent at most core locations
525 (Table 2). Correlations to sea ice extent are (even) weaker than those for sea ice area and consequently not
526 shown. We performed a lead-lag study of the correlations between Φ and sea ice area/extent in the various
527 sectors, and find that in all cases maximum correlations occur for the sea ice changes lagging 0 to 4 months
528 behind Φ ; we interpret this to mean that the sea ice is responding to changes in atmospheric circulation,
529 rather than driving them.

530 Overall, we find that synoptic activity at WAIS Divide, the site of most interest here, is controlled by the
531 position and/or strength of the stormtracks at the southern edge of the SPJ in the Pacific sector of the
532 Southern Ocean (Ross, Amundsen and Bellingshausen Seas), with little sensitivity to the SPJ behavior in
533 the other sectors. Owing to its remote southern location, WDC is only weakly impacted by the commonly-
534 defined large-scale modes of atmospheric variability. Most notably, WDC has a modest influence from the
535 tropical Pacific climate, as shown by a correlation around $r \approx 0.3$ to the PSA1, Niño 3.4 and PDO indices
536 (Table 2). We further find statistically significant correlations (up to $r = 0.44$) between WDC Φ and SST
537 in broad regions of the central and eastern tropical Pacific (not shown). We suggest that ENSO weakly
538 impacts storminess at WDC (around 10% of variance explained) via its impact on the SPJ in the South
539 Pacific.

540 **5 Barometric variability in West Antarctica during the last deglaciation**

541 **5.1 The 0-24 ka WAIS Divide Kr-86 excess record**

542 The WAIS Divide downcore $^{86}\text{Kr}_{\text{xs}}$ dataset we present here was produced during five separate measurement
543 campaigns that occurred in February-April 2014, February-April 2015, August 2015, August 2020, and
544 August 2021, respectively. Campaigns 1-3 were reported previously (Bereiter et al., 2018a; Bereiter et al.,
545 2018b), and campaigns 4 and 5 were meant to resolve conflicts between the $^{86}\text{Kr}_{\text{xs}}$ data sets from these
546 earlier campaigns. Three slightly different measurement approaches were used. Campaign 1 uses “Method
547 1” from Bereiter et al. (2018a), in which the air sample splitting is done in a water bath for over 12 hours
548 to equilibrate the sample. Campaigns 2 and 3 use “Method 2” from Bereiter et al. (2018a), in which a
549 bellows is used to split the air samples for over 4 to 6 hours. Campaigns 4 and 5 do not involve splitting of
550 the air sample, and only analyzed the Kr and Ar isotopic ratios. During campaign 4 a glass bead from the
551 water trap had gotten stuck in the tubing, restricting the flow and likely resulting in incomplete air extraction
552 from the melt water.

553 Figure 6 compares $^{86}\text{Kr}_{\text{xs}40}$ (panel A) and $^{86}\text{Kr}_{\text{xs}15}$ (panel B) from the five campaigns. Campaign 1 is the
554 only campaign that spans the full age range of the record, making it the most valuable of the three
555 campaigns. Campaigns 2 and 3 are mostly restricted to the Pleistocene and Holocene periods respectively,
556 with little overlap between them. Campaigns 4 and 5 aimed to reproduce some of the most salient features
557 in the earlier three. For ease of visual comparison, a Gaussian smoothing spline to the combined data from
558 the two most extensive campaigns (1 and 2) is added (details below).

559 Visual inspection suggests that campaigns 1 and 2 agree well for both $^{86}\text{Kr}_{\text{xs}}$ definitions; campaign 3 has
560 more scatter and is visibly offset (more negative) for both $^{86}\text{Kr}_{\text{xs}}$ definitions; campaign 4 has several data
561 points that agree well with the spline, yet also several fliers with very negative $^{86}\text{Kr}_{\text{xs}40}$; campaign 5 appears
562 overall more negative in $^{86}\text{Kr}_{\text{xs}40}$. No true replicate samples were analyzed between the campaigns, in part
563 because the large sample size requirement precludes this. This precludes a direct assessment of campaign
564 offsets. Instead we rely on linear interpolation. First, we linear interpolate the $^{86}\text{Kr}_{\text{xs}}$ values of campaign 1
565 onto the sample depths of campaign 2, and vice versa, allowing us to estimate the offsets. In this way,
566 during their period of overlap we estimate offsets of 6 and 13 per meg $\%^{-1}$ between campaigns 1 and 2 for
567 $^{86}\text{Kr}_{\text{xs}40}$ and $^{86}\text{Kr}_{\text{xs}15}$, respectively. This is within the analytical precision (22 per meg), suggesting these two
568 campaigns are in good agreement. Data from campaign 2 appear to have more scatter, possibly reflecting
569 the shorter equilibration time during sample splitting.

570 We combine data from the first two campaigns, and evaluate their offset to data from the other three
571 campaigns again using the linear interpolation method. For campaigns 3, 4 and 5 we find an offset of -32,
572 -22 and -23 per meg $\%^{-1}$ in $^{86}\text{Kr}_{\text{xs}40}$, respectively. For campaign 3 the offset is -34 per meg $\%^{-1}$ in $^{86}\text{Kr}_{\text{xs}15}$.
573 It is remarkable that all three later campaigns are more negative in $^{86}\text{Kr}_{\text{xs}}$ than the first two. Campaign 3
574 shows the greatest offset (greater than analytical precision), and has more scatter in both $^{86}\text{Kr}_{\text{xs}}$ (Fig. 6) and
575 ^{15}N excess, possibly because for this campaign less care was taken that the IRMS conditions were stable.
576 The offset of campaign 4 may be attributed to the incomplete sample transfer due to the bead stuck in the
577 line; note that for this campaign the offset is caused by two very negative data points. The offset in campaign
578 5 is hard to explain. The more negative $^{86}\text{Kr}_{\text{xs}}$ of campaigns 4 and 5 may reflect sample storage effects, as
579 these were measured 5-6 years after campaign 1 and 2. However this would not explain the negative values

580 of campaign 3. The good $^{86}\text{Kr}_{\text{xs}}$ agreement between DE08 and DE08-OH, drilled 32 years apart, would also
581 argue against large storage effects. For campaign 4 and 5 only Ar and Kr isotope ratios were measured, and
582 so we lack typical tracers of gas loss ($\delta\text{O}_2/\text{N}_2$ and $\delta\text{Ar}/\text{N}_2$) that can be analyzed.

583 In the remainder of this paper we will interpret the combined data from campaigns 1 and 2, but with the
584 caveat that there is a persistent offset with later campaigns. However, the features we interpret are
585 corroborated by the later campaigns, if one takes the offset into account. To aid interpretation of the data,
586 we apply a Gaussian smoothing spline with a smoothing filter width that varies depending on the data
587 density (from 250-year width in the deglaciation itself where the data density is high, to 1750 years in the
588 Holocene and LGM where data density is low). To estimate the uncertainty in the smoothing spline we use
589 a Monte Carlo approach that considers uncertainty in (1) the gas loss correction, by randomly sampling ϵ_{40}
590 in the range of 0 to -0.016, and by randomly adding an offset in the range of -1‰ to +1‰ to the gas loss
591 indicator ($\delta\text{O}_2/\text{N}_2 - \delta\text{Ar}/\text{N}_2$); (2) the thermal correction, by randomly scaling the thermal scenario (Fig. A5)
592 by a factor ranging from 0 to 2; and (3) analytical errors, by adding random errors to individual data points
593 drawn from a normal distribution with a 2σ width of 22 per meg. The $\pm 1\sigma$ uncertainty range with mean
594 value are shown as the gray envelope and center line in Fig. 6. We believe the following observations to be
595 robust:

- 596 • The Holocene shows a trend towards increasingly negative $^{86}\text{Kr}_{\text{xs}}$, suggesting a gradual increase in
597 synoptic activity toward the present. Minimum synoptic activity in West Antarctica occurs during the
598 early Holocene around 10 ka BP; the Monte Carlo study suggests $^{86}\text{Kr}_{\text{xs}40}$ in the early Holocene (8ka-
599 10ka BP) is 30.5 ± 18 per meg ‰^{-1} ($\pm 2\sigma$) below the late-Holocene value (last 2 ka). Using the slope of
600 our core-top calibration (Fig. 3), we estimate that early-Holocene WDC synoptic activity Φ is $\sim 17\%$
601 weaker than it is today. This change is comparable to the 2σ magnitude of interannual variations in
602 annual mean Φ at the site today (or about half the peak-to-peak variations thereof). This Holocene trend
603 is seen in the data from campaigns 1, 3 and 4. Campaign 5 does not suggest a trend but has only one
604 late Holocene data point making it less robust. The trend in campaign 3 is less robust due to the greater
605 scatter in the data.
- 606 • The most pronounced change occurs at the Younger Dryas (YD) - Holocene transition, where $^{86}\text{Kr}_{\text{xs}}$
607 becomes more positive (by 30.1 ± 16 per meg ‰^{-1} , comparing YD and early Holocene) implying a
608 decrease in synoptic activity. This transition is observed in campaigns 1, 2, 4 and 5 that cover this time
609 period (the third campaign does not cover it), and represents a $\sim 17\%$ drop in synoptic activity (Φ).
- 610 • During the Last Glacial Maximum (LGM), WDC synoptic activity was perhaps slightly weaker than at
611 present, but not significantly so ($^{86}\text{Kr}_{\text{xs}40}$ more positive by 11 ± 13 per meg ‰^{-1}). The West Antarctic
612 ice sheet elevation was likely higher during the LGM, and a 300 m elevation increase would by itself
613 increase $^{86}\text{Kr}_{\text{xs}40}$ by 10 per meg ‰^{-1} , all else being equal (Appendix A3); this is within the analytical
614 error of our observations. This feature is seen in campaign 1 and not covered by the other campaigns.
- 615 • The deglaciation itself has enhanced synoptic activity, in particular during the two North-Atlantic cold
616 stages Heinrich Stadial 1 (HS1) and the YD as highlighted with yellow bars in Figs. 6 and 7. Synoptic
617 activity during these periods is enhanced relative to the adjacent LGM and early Holocene, yet
618 comparable to today. This feature is seen in campaigns 1 and 2, and in 4 and 5 for the transition into
619 the Holocene.

620 Below we will interpret the deglacial WDC $^{86}\text{Kr}_{\text{xs}}$ record in terms of time-averaged barometric variability.
621 Before doing so we want to emphasize that firn processes may have been imprinted onto the record also, in
622 particular on orbital timescales where firn microstructure responds to local (summer) insolation intensity
623 (Bender, 2002). High summer insolation results in more depleted $\delta\text{O}_2/\text{N}_2$ and reduced air content, likely via
624 stronger layering and a delayed pore close-off process (Fujita et al., 2009).

625 Local summer solstice insolation in Antarctica increases through the Holocene, with the highest values in
626 the late Holocene. This may impact $^{86}\text{Kr}_{\text{xs}}$, although it is not a-priori clear what the sign of this relationship
627 would be. The sense of the Holocene temporal trends is that a more negative $^{86}\text{Kr}_{\text{xs}}$ coincides with more
628 negative $\delta\text{O}_2/\text{N}_2$. Note that this is opposite to the trends seen in the spatial calibration, where sites with the
629 most negative $\delta\text{O}_2/\text{N}_2$ (DF, SP, EDC) have the most positive $^{86}\text{Kr}_{\text{xs}}$. For now, the impact of local insolation
630 on $^{86}\text{Kr}_{\text{xs}}$ via firn microstructure remains unknown, which is an important caveat in interpreting the orbital-
631 scale changes in WDC $^{86}\text{Kr}_{\text{xs}}$. The abrupt $^{86}\text{Kr}_{\text{xs}}$ increase at the Holocene onset is too abrupt to be caused by
632 insolation changes, and thus we can interpret that change with more confidence.

633 The scatter in the late Holocene WDC $^{86}\text{Kr}_{\text{xs}}$ data exceeds the stated analytical precision. Potential
634 explanations include (1) an underestimation of the true analytical precision; (2) interannual to decadal
635 variations in storminess at WDC; and (3) aliasing of cm-scale variations in ice core $^{86}\text{Kr}_{\text{xs}}$ linked to layering
636 in firn microstructural properties. Understanding the cause of this relatively high scatter in the $^{86}\text{Kr}_{\text{xs}}$ records
637 will require more work, in particular the measurements of several high resolution $^{86}\text{Kr}_{\text{xs}}$ records in various
638 sectors of Antarctica.

639 **5.2 Barometric variability at WAIS Divide during the last deglaciation**

640 In the present-day, synoptic-scale pressure variability at WAIS Divide is correlated with zonal wind
641 strength along the southern margin of the SPJ (Section 4). In our interpretation, a more negative $^{86}\text{Kr}_{\text{xs}}$
642 reflects a strengthening or southward shift of the SPJ in the Pacific sector. Here we provide a climatic
643 interpretation of the deglacial WDC $^{86}\text{Kr}_{\text{xs}}$ record, and suggest that variations in synoptic variability at WDC
644 are linked to meridional movement of the ITCZ on millennial and orbital timescales.

645 The main features of the deglacial WDC $^{86}\text{Kr}_{\text{xs}}$ record listed in Section 5.1 resemble similar features seen
646 in records of (sub-) tropical hydrology and monsoon strength, such as the speleothem calcite $\delta^{18}\text{O}$ records
647 from Hulu Cave, China (Fig. 7C) and from Botuvera cave, southern Brazil (Fig. 7D), which are thought to
648 reflect the intensity of the East Asian and South American summer monsoons, respectively (Cruz et al.,
649 2005; Wang et al., 2007; Wang et al., 2001). These two monsoon records are anti-correlated, showing
650 opposing rainfall trends between the NH and SH on both orbital and millennial timescales. This pattern is
651 commonly attributed to displacement of the mean meridional position of the ITCZ (Chiang and Friedman,
652 2012; McGee et al., 2014; Schneider et al., 2014), driven by hemispheric temperature differences (Fig. 7B).
653 On orbital timescales such ITCZ migration has a strong precessional component, moving towards the
654 hemisphere with more intense summer peak insolation; on millennial timescales the ITCZ responds to
655 abrupt North-Atlantic climate change associated with the D-O and Heinrich cycles (Broccoli et al., 2006;
656 Chiang and Bitz, 2005; Wang et al., 2001), which are in turn linked to changes in meridional heat transport
657 by the Atlantic meridional overturning circulation, or AMOC (Lynch-Stieglitz, 2017; Rahmstorf, 2002).

658 Changes in mean ITCZ position have a strong influence on the structure and strength of the SH jets. During
659 periods when the NH is relatively cold (such as D-O stadials or periods with negative orbital precession
660 index) the ITCZ is displaced southward and the SH Hadley cell is weakened, thereby also weakening the
661 SH upper-tropospheric subtropical jet (Ceppi et al., 2013; Chiang et al., 2014). The reverse is also true, with
662 the ITCZ shifted northward during NH warmth, associated with a strengthening of the SH Hadley cell and
663 STJ. In a range of model simulations (Ceppi et al., 2013; Lee and Kim, 2003; Lee et al., 2011; Pedro et al.,
664 2018) the weakening of the SH STJ (as during NH cold) is furthermore accompanied by a strengthening
665 and/or southward shift of the SPJ/eddy-driven jet and SH westerly winds. Recently, ice core observations
666 have confirmed in-phase shifts in the position of the SHW occur during the D-O cycle in parallel to those
667 of the ITCZ (Buizert et al., 2018; Markle et al., 2017). Marine records of fluvial sediment runoff off the
668 Chilean coast suggest precession-phased movement of the South Pacific SPJ, again in parallel to the ITCZ
669 movement (Lamy et al., 2019).

670 The SAM index reflects the meridional position of the SHW and eddy-driven jet. During positive SAM
671 phases the SHW are displaced poleward, and during negative phases equatorward. Present-day month-to-
672 month changes in SAM index represent a mode of internal variability, with anomalies persisting for only
673 weeks to months – the timescale is longest in late spring and early summer reflecting a stronger planetary
674 wave–mean flow interaction (Simpson et al., 2011; Thompson and Wallace, 2000). By contrast, shifts in
675 the ITCZ and SH jet structure on millennial and orbital timescales have a much longer lifetime and different
676 dynamics, being driven from the tropics via hemispherically asymmetric changes in Hadley cell and STJ
677 strength. Therefore, present-day SAM internal variability is not expected to be a good analogue for past
678 changes in SHW position. We find that the present-day SAM month-to-month internal variability mainly
679 impacts synoptic variability over the Southern Ocean and does not have a statistically significant impact at
680 WDC (Table 2). Such variability is likely to have occurred during other climatic regimes also, possibly just
681 centered around a mean SHW position that is displaced meridionally relative to today. At first glance it
682 may appear contradictory to state, as we do, that synoptic activity at WDC is not sensitive to the SAM while
683 also suggesting that during the last deglaciation synoptic activity at WDC is linked to changes in the position
684 of the SH eddy-driven jet and westerlies. Based on the considerations above, both claims may be true
685 without contradiction.

686 Besides secular changes to the SPJ position/strength linked to meridional ITCZ movement, WDC $^{86}\text{Kr}_{\text{xs}}$
687 may also have imprints from ENSO and tropical Pacific climate. Our analysis suggests a weak, but
688 statistically significant link to common ENSO indicators (Table 2). Increased synoptic activity at WDC is
689 linked to enhanced convection in the central and eastern tropical Pacific, which may be due to enhanced
690 frequency or intensity of El Niño events, or a mean climate state that is more El Niño-like; it seems likely
691 that the Pacific mean state and ENSO variability are strongly linked (Salau et al., 2012), and the distinction
692 may be irrelevant.

693 The key features of the WDC $^{86}\text{Kr}_{\text{xs}}$ record are compatible with paleo-ENSO changes commonly described
694 in the literature. A majority of Holocene ENSO reconstructions (Conroy et al., 2008; Driscoll et al., 2014;
695 Koutavas et al., 2006; Moy et al., 2002; Riedinger et al., 2002; Sadekov et al., 2013) and a wide range of
696 climate model simulations (Braconnot et al., 2012; Cane, 2005; Clement et al., 2000; Liu et al., 2000; Liu
697 et al., 2014; Zheng et al., 2008) all suggest weakened ENSO activity during the early and mid-Holocene, a
698 time with reduced WDC synoptic activity. For example, Fig. 7F shows the number of El Niño events per
699 century (with trend line) reconstructed from inorganic clastic laminae in sediments from Laguna

700 Pallacocha, Ecuador, a region strongly affected by ENSO (Moy et al., 2002). Likewise, it has been
701 suggested that the SST gradient between the West Pacific warm pool and East Pacific cold tongue was
702 enhanced during the mid-Holocene, perhaps indicating a more La Niña-like mean climate state (Koutavas
703 et al., 2002; Sadekov et al., 2013).

704 Going from the early Holocene to the Younger Dryas (YD), we observe a large increase in WDC synoptic
705 activity. Enhanced ENSO activity during Heinrich stadials is generally supported by climate model
706 simulations (Braconnot et al., 2012; Merkel et al., 2010; Timmermann et al., 2007), and by limited proxy
707 evidence for stadial periods more broadly (Stott et al., 2002). Enhanced ENSO variability during the
708 deglaciation is also found by Sadekov et al. (2013), although their record lacks the temporal resolution to
709 resolve the individual stages. The zonal SST gradient in the equatorial Pacific further reaches a minimum
710 during HS1, also consistent with higher El Niño intensity (Sadekov et al., 2013).

711 The observed variations in $^{86}\text{Kr}_{\text{xs}}$ and implied changes in WDC synoptic activity may thus have two
712 contributions: (1) ITCZ-driven changes to the South Pacific SPJ position, and (2) changes to ENSO activity.
713 Based on previous work, we argue these two amplify one another in driving WDC storminess, yet we expect
714 the former to make the larger contribution. To disentangle zonally-uniform changes to the SPJ from changes
715 specific to the Pacific sector (such as ENSO and the split jet), $^{86}\text{Kr}_{\text{xs}}$ records from different sectors of
716 Antarctica are needed. Replication of the deglacial and Holocene WDC $^{86}\text{Kr}_{\text{xs}}$ record presented here is also
717 a high priority, both at WDC itself and at the nearby SDM and RICE cores, to validate that the signals we
718 describe and interpret here are indeed real and regional in scale.

719 The position of the SHW during the LGM has been a topic of much scientific inquiry. Proxy data have been
720 interpreted to show a northward LGM shift of the SHW – with other scenarios, including no change at all,
721 not excluded by the data (Kohfeld et al., 2013). Such a shift is not supported by most climate models (Rojas
722 et al., 2009; Sime et al., 2013). Our $^{86}\text{Kr}_{\text{xs}}$ record suggests LGM synoptic activity in West Antarctica to be
723 comparable to today after accounting for site elevation effects (the elevation effect on $^{86}\text{Kr}_{\text{xs}}$ is within the
724 analytical error). This would be consistent with a Pacific SPJ position similar to today. Note that our site is
725 mostly sensitive to the position of the southern edge of the SPJ, and cannot meaningfully constrain changes
726 to the seasonality, width, and/or northern edge of the stormtracks. Therefore, it is not a-priori clear whether
727 our observations can be extrapolated to more general statements about SHW position and strength during
728 the LGM. Our data suggest that SPJ movement follows insolation and the ITCZ position, and hence the
729 LGM period may not be a good target for studying SHW movement in the first place given that it has a
730 precession index similar to the present-day.

731 Changes to the SPJ and its associated westerly surface winds have implications for ocean circulation and
732 marine productivity in the Southern Ocean via wind-driven upwelling. Opal flux records from the Antarctic
733 zone (Fig. 7G), reflecting diatom productivity, are commonly interpreted as a proxy for such upwelling –
734 with enhanced upwelling during southward displacement of the SHW (Anderson et al., 2009). Here we
735 only show records from the Pacific sector, given we find WDC $^{86}\text{Kr}_{\text{xs}}$ to reflect purely local SPJ dynamics
736 (Fig. 4A). Both published records suggest enhanced upwelling during the deglaciation (Fig. 7G), consistent
737 with a southward-shifted Pacific SPJ and enhanced storminess at WDC. The record from core PS75/072-4
738 (blue curve) further indicates an increasing productivity trend through the Holocene (Studer et al., 2018),
739 which is accompanied by a rise in surface nitrogen availability (reconstructed from diatom-bound nitrogen
740 isotopic composition, not shown); this Holocene trend matches our finding of increasing WDC storminess

741 and, by inference, an increasingly southern position of the Pacific SPJ and SHW. We thus conclude that
742 our interpretation of WDC $^{86}\text{Kr}_{\text{xs}}$ reflecting SPJ movement in parallel with the ITCZ, is broadly consistent
743 with indicators of wind-driven upwelling in the Pacific Antarctic zone.

744 **6 Conclusions**

745 Here we present a new gas-phase ice core climate proxy, Kr-86 excess, that reflects time-averaged surface
746 pressure variability at the site driven by synoptic activity. Surface pressure variability weakly disturbs the
747 gravitational settling and enrichment of the noble gas isotope ratios $\delta^{86}\text{Kr}$ and $\delta^{40}\text{Ar}$ via barometric
748 pumping. Owing to its higher diffusion coefficient, argon is less affected by this process than krypton is,
749 and therefore the difference $\delta^{86}\text{Kr}-\delta^{40}\text{Ar}$ is a measure of synoptic activity.

750 This interpretation is supported by a calibration study in which we measure $^{86}\text{Kr}_{\text{xs}}$ in late Holocene ice core
751 samples from eleven Antarctic and one Greenland ice core that represent a wide range of synoptic activity
752 in the modern climate. Two of the Antarctic cores were rejected due to clear evidence of refrozen melt
753 water. We find a strong correlation ($r = -0.94$ when using site mean data and $r = -0.83$ when using individual
754 samples, $p < 0.01$) between ice core $^{86}\text{Kr}_{\text{xs}}$ and barometric variability at the site.

755 Current limitations of the new $^{86}\text{Kr}_{\text{xs}}$ proxy are: (1) it requires relatively large and non-trivial corrections
756 for gas loss and thermal fractionation; (2) it is moderately sensitive to changes in convective zone thickness;
757 (3) firn air transport models cannot simulate the magnitude of $^{86}\text{Kr}_{\text{xs}}$ anomalies measured in ice samples;
758 (4) firn air samples show smaller $^{86}\text{Kr}_{\text{xs}}$ anomalies than ice samples from the same site do; (5) it may be
759 sensitive to the degree of density layering at the site, as a comparison of the nearby Law Dome DE08 and
760 DSSW20K cores suggests; (6) it does not work for warm sites that experience frequent melt; (7) the
761 measurement is challenging (with offsets observed between measurement campaigns), time consuming,
762 and needs large ice samples; and (8) long-term sample storage may impose data offsets. Due to these
763 limitations, we caution that any interpretation of temporal $^{86}\text{Kr}_{\text{xs}}$ changes remains speculative at present.

764 Using atmospheric reanalysis data, we show that synoptic-scale barometric variability in Antarctica is
765 primarily linked to the position and/or strength of the southern edge of the eddy-driven subpolar jet (SPJ,
766 also called polar front jet) with a southward SPJ displacement enhancing synoptic-scale surface pressure
767 variability in Antarctica. The commonly-defined modes of large-scale atmospheric variability, such as the
768 southern annular mode and the Pacific-South American pattern, impact Antarctic only weakly as they are
769 weighted towards the mid-latitudes; the exception is the Antarctic Peninsula, where synoptic activity is
770 well-correlated with the southern annular mode ($r = 0.68$). Sites in the Amundsen and Ross Sea sectors are
771 weakly linked to tropical Pacific climate and ENSO ($r = 0.31$ to $r = 0.43$).

772 We present a new record of $^{86}\text{Kr}_{\text{xs}}$ from the WAIS Divide ice core in West Antarctica, that covers the last
773 24ka including the LGM, deglaciation and Holocene. West Antarctic synoptic activity is slightly below
774 modern levels during the last glacial maximum (LGM); increases during the Heinrich Stadial 1 and Younger
775 Dryas North Atlantic cold periods; weakens abruptly at the Holocene onset; remains low during the early
776 and mid-Holocene (up to $\sim 17\%$ below modern), and gradually increases to its modern value. The WDC
777 $^{86}\text{Kr}_{\text{xs}}$ record resembles records of tropical hydrology and monsoon intensity that are commonly thought to
778 reflect the meridional position of the ITCZ; the sense of the correlation is that WDC synoptic activity is
779 weak when the ITCZ is in its northward position, and vice versa. We interpret the record to reflect
780 migrations of the eddy-driven SPJ in parallel with those of the ITCZ (Ceppi et al., 2013). Secondary
781 influences may come from tropical Pacific climate and ENSO activity. Our $^{86}\text{Kr}_{\text{xs}}$ record is consistent with
782 weakened ENSO activity (or a more La Niña-like mean state) during the mid- and early Holocene, and
783 enhanced ENSO activity during NH stadial periods – both these features have been described in the paleo-

784 ENSO literature. The inferred changes to the SPJ are broadly consistent with proxies that indicate enhanced
785 wind-driven upwelling in the Pacific Antarctic zone during NH cold stadial periods.

786 Kr-86 excess is a new and potentially useful ice core proxy with the ability to enhance our understanding
787 of past atmospheric circulation. More work to better understand this proxy is warranted, and presently the
788 conclusions of this paper should be considered as tentative. In particular, replication of the deglacial Kr-86
789 excess record presented here in nearby cores is needed before these results can be interpreted with
790 confidence. A full list of suggested follow-up studies is given in section 3.3. Despite the many challenges
791 of Kr-86 excess, its further development is worthwhile owing to the dearth of available proxies for
792 reconstructing SH extratropical atmospheric circulation.

793 Appendix A: data corrections

794 A1 Gas loss correction

795 Gas loss processes artificially enrich the $\delta^{40}\text{Ar}$ isotopic ratio used to calculate $^{86}\text{Kr}_{\text{xs}}$ (Kobashi et al., 2008b;
796 Severinghaus et al., 2009; Severinghaus et al., 2003). Figure A1B shows the relationships between the two
797 most common gas loss proxies $\delta\text{O}_2/\text{N}_2$ and $\delta\text{Ar}/\text{N}_2$ for all samples in the calibration dataset; we find a slope
798 close to the 2:1 slope commonly reported in the literature (Bender et al., 1995); the exception is the DE08-
799 OH site where the data fall on a 1:1 slope. Depletion in fugitive gases (such as O_2 and Ar) represents the
800 sum of losses during bubble closure in the firn (Bender, 2002; Huber et al., 2006; Severinghaus and Battle,
801 2006), and those during drilling, handling, storage, and analysis of the samples (Ikeda-Fukazawa et al.,
802 2005). The patterns are inconsistent with storage conditions alone – for example the DF and EDC cores
803 were stored very cold and SP drilled very recently; yet all three have strong $\delta\text{O}_2/\text{N}_2$ and $\delta\text{Ar}/\text{N}_2$ depletion.
804 Natural gas loss from the firn, as well as artefactual loss during drilling likely dominate the signal. The
805 DE08-OH samples were dry-drilled and suffered from poor ice quality for the most depleted samples, which
806 may explain the alternate 1:1 slope at the site (Appendix B); note though that a recent work suggests a $\sim 5:1$
807 slope for post-coring gas loss (Oyabu et al., 2021). The DE08-OH samples were also analyzed differently
808 from those at other sites, with $\delta\text{O}_2/\text{N}_2$ and $\delta\text{Ar}/\text{N}_2$ measurements performed on a separate smaller ice piece
809 (see section 2.2); the greater surface-to-volume ratio of such small samples may result in greater gas
810 fractionation while evacuating the sample flasks in the laboratory.

811 Severinghaus et al. (2009) hypothesize that the apparent 2:1 slope of $\delta\text{O}_2/\text{N}_2$ to $\delta\text{Ar}/\text{N}_2$ depletion is a
812 combination of two mechanisms: size-dependent fractionation during diffusion through the ice lattice, and
813 mass-dependent fractionation (such as molecular or Knudsen diffusion) within ice fractures. In this
814 interpretation, the exact slope would depend on the relative contribution of each process to the total gas
815 loss. It is improbable that both processes would occur in the same ratio at such a wide variety of sites; the
816 2:1 slope is thus more likely an attribute of the gas diffusion rate of gases through ice itself, which is strongly
817 size-dependent, and weakly mass-dependent (Battle et al., 2011).

818 Gas loss is well known to enrich ice samples in $\delta^{18}\text{O}-\text{O}_2$, and following Severinghaus et al. (2009) we plot
819 $\delta^{18}\text{O}$ (corrected for gravity and small atmospheric $\delta^{18}\text{O}_{\text{atm}}$ variations) against gravitationally-corrected
820 $\delta\text{O}_2/\text{N}_2$ in Fig. A1C. We find a slope of 3.5 per meg enrichment in $\delta^{18}\text{O}$ per ‰ of $\delta\text{O}_2/\text{N}_2$ gas loss. This is
821 less than values reported elsewhere (Severinghaus et al., 2009), but provides further evidence for mass-
822 dependent fractionation during gas loss. Our core top dataset further suggests a correlation between
823 $\delta^{40}\text{Ar} - 4 \times \delta^{15}\text{N}$ (a measure of $\delta^{40}\text{Ar}$ enrichment impacted by both thermal fractionation and gas loss) and
824 gravitationally corrected $\delta\text{Ar}/\text{N}_2$ (Fig. A1D), suggesting Ar loss leads to enrichment of the remaining $\delta^{40}\text{Ar}$.

825 Following Severinghaus et al. (2009), we assume that the $\delta^{40}\text{Ar}$ correction scales with gas loss indicator
826 ($\delta\text{O}_2/\text{N}_2 - \delta\text{Ar}/\text{N}_2$):

$$827 \quad \Delta_{GL}^{40} = \varepsilon_{40} \times (\delta\text{O}_2/\text{N}_2 - \delta\text{Ar}/\text{N}_2)|_{\text{gravcorr}} \quad (\text{A1})$$

828 with Δ_{GL}^{40} the isotopic gas loss correction on $\delta^{40}\text{Ar}$ and ε_{40} a scaling parameter. Note that gravitationally
829 corrected $\delta\text{O}_2/\text{N}_2$ and $\delta\text{Ar}/\text{N}_2$ data are used. Here we rely on data from the Antarctic Byrd ice core for a best

830 estimate of ϵ_{40} (Fig. A2); some samples from this core suffered extreme gas loss with $(\delta O_2/N_2 - \delta Ar/N_2)$ as
 831 low as -100%. This data set suggest $\epsilon_{40} = -0.008$, or 8 per meg $\delta^{40}Ar$ enrichment per ‰ of $(\delta O_2/N_2 - \delta Ar/N_2)$
 832 gas loss. Because of the 2:1 slope between $\delta O_2/N_2$ and $\delta Ar/N_2$, we find that $(\delta O_2/N_2 - \delta Ar/N_2) \approx \delta Ar/N_2$
 833 and therefore the coefficient ϵ_{40} would have a similar slope when regressed against $\delta Ar/N_2$ instead of
 834 $(\delta O_2/N_2 - \delta Ar/N_2)$.

835 The value of $\epsilon_{40} = -0.008$ agrees reasonably well with other studies. Kobashi et al. (2008) compare replicate
 836 sample pairs to back out gas loss, and find (statistically significant) correlations between $\delta^{40}Ar$ enrichment
 837 and $\delta Ar/N_2$ (again, which is similar to $\delta O_2/N_2 - \delta Ar/N_2$). Kobashi et al. (2008) find ϵ_{40} values of -0.006, -
 838 0.005 and +0.007, depending on the depth range and analytical campaign evaluated. The positive value is
 839 surprising, given that most observations, as well as theory, suggest ϵ_{40} should be negative – we consider
 840 this a spurious result given the weak $\delta^{40}Ar - \delta Ar/N_2$ correlation in that particular data set. The other two
 841 values of ϵ_{40} are in reasonable agreement with the Byrd value. For the Siple Dome ice core (Severinghaus
 842 et al., 2003), regressing $\delta^{40}Ar$ against $\delta Kr/Ar$ gives a slope of +0.007; this implies $\epsilon_{40} = -0.007$ in good
 843 agreement with our findings. Last, our coretop data suggest $\delta^{40}Ar$ enrichment with an ϵ_{40} value of -0.0072
 844 (Fig. A1D), also in good agreement with Byrd.

845 Given the uncertainty in the gas loss parameter, we verify that our results are valid for a wide range of ϵ_{40}
 846 values (Fig. 3B).

847 The downcore WDC $^{86}Kr_{xs}$ was measured over five separate measurement campaigns, with $\delta O_2/N_2$ and
 848 $\delta Ar/N_2$ data available only for the first three campaigns.

849 In order to provide a consistent gas loss correction to the five measurement campaigns, including campaigns
 850 4 and 5 for which no $\delta O_2/N_2$ or $\delta Ar/N_2$ data are available, we fit a third-order polynomial to all available
 851 gravitationally-corrected WDC $\delta O_2/N_2 - \delta Ar/N_2$ data (Fig. A5A). We can then calculate the expected WDC
 852 $\delta O_2/N_2 - \delta Ar/N_2$ at any given age, also in the absence of $\delta O_2/N_2$ and $\delta Ar/N_2$ data. For consistency, we use
 853 this correction method for all data seen in Fig. 6. Note that the WDC $\delta O_2/N_2 - \delta Ar/N_2$ values are small for
 854 all ages, and that therefore the gas loss correction is small for this site.

855 A2 Thermal correction

856 In the presence of a temperature gradient, thermal diffusion causes isotopic enrichment towards the colder
 857 location. The thermal diffusion sensitivity Ω in units of ‰K⁻¹ for the various gases is given as (Grachev
 858 and Severinghaus, 2003a, b; Kawamura et al., 2013):

$$859 \quad \Omega^{15} = \frac{8.656}{T} - \frac{1232}{T^2}$$

$$860 \quad \Omega^{40} = \frac{26.08}{T} - \frac{3952}{T^2}$$

$$861 \quad \Omega^{86} = \frac{5.05}{T} - \frac{580}{T^2}$$

862 We estimate the thermal gradient ΔT in the firn using N-15 excess (Severinghaus et al., 1998):

$$863 \quad \Delta T = \frac{{}^{15}\text{N}_{xs}}{\Omega^{15} - \Omega^{40}/4} = \frac{\delta^{15}\text{N} - (\delta^{40}\text{Ar} + \Delta_{GL}^{40})/4}{\Omega^{15} - \Omega^{40}/4} \quad (\text{A2})$$

864 with Δ_{GL}^{40} the $\delta^{40}\text{Ar}$ gas loss correction from Eq. (A1). Positive values of ΔT indicate that the surface is
865 warmer than the firn-ice transition. The ΔT then in turn allows us to estimate the thermal corrections:

$$866 \quad \Delta_{TF}^{15} = -\Omega^{15} \Delta T$$

$$867 \quad \Delta_{TF}^{40} = -\Omega^{40} \Delta T$$

$$868 \quad \Delta_{TF}^{86} = -\Omega^{86} \Delta T \quad (\text{A3})$$

869 The samples from the calibration dataset are from the climatically stable late Holocene period, and typically
870 close together in depth; the uncertainty in the ΔT estimation for individual samples therefore exceeds the
871 temporal variability in ΔT . To reduce the uncertainty in the thermal correction we estimate ΔT for individual
872 samples using Eq. (A2), and for each site average the available data to get a site-average firn temperature
873 gradient $\overline{\Delta T}$. The thermal correction is then given by:

$$874 \quad \Delta_{TF}^{15} = -\Omega^{15} \overline{\Delta T}$$

$$875 \quad \Delta_{TF}^{40} = -\Omega^{40} \overline{\Delta T}$$

$$876 \quad \Delta_{TF}^{86} = -\Omega^{86} \overline{\Delta T} \quad (\text{A4})$$

877 The two methods are compared in Figs. A3C (individual sample ΔT) and A3D (site mean $\overline{\Delta T}$); it is clear
878 that the $\overline{\Delta T}$ approach reduces the spread in ${}^{86}\text{Kr}_{xs}$ (error bars), but not its mean (white dots). The ΔT estimates
879 in individual samples are subject to errors in the isotopic measurements; some of these errors will cancel
880 out in the $\overline{\Delta T}$.

881 For the downcore WDC record through the deglaciation we can no longer assume a stationary ΔT ; we
882 instead rely on dynamic firn densification model simulations of ΔT (Buizert et al., 2015). A comparison of
883 the simulated and data-based ΔT is shown in Fig. A5 for WDC. The data clearly show a lot more
884 scatter/variability than the simulations do. We interpret this mainly as analytical noise in the $\delta^{15}\text{N}$ and $\delta^{40}\text{Ar}$
885 measurements, however, the gas loss correction (Appendix A1) also impacts the ΔT estimation in individual
886 samples. The comparison suggests that the scatter in the ΔT estimates actually exceeds the magnitude of
887 the simulated thermal signals. Using ΔT of the individual samples would thus introduce much scatter in the
888 (thermally corrected) ${}^{86}\text{Kr}_{xs}$ records, and we choose to use the modelled ΔT instead.

889 **A3 Elevation correction**

890 To correct the deglacial WAIS Divide record for elevation changes, we here estimate the $^{86}\text{Kr}_{\text{xs}}$ dependence
891 on site elevation using the calibration dataset. Note that elevation and synoptic activity are strongly
892 correlated for the investigated sites ($r = -0.86$), with synoptic activity decreasing with elevation because
893 the cyclonic systems do not penetrate deeply into the Antarctic interior. Figure A6 shows the result of this
894 exercise. We find a slope of 34 per meg $\%^{-1}$ of $^{86}\text{Kr}_{\text{xs}}$ per 1000 m of elevation change, with a correlation of
895 $r = 0.96$ when considering site-mean $^{86}\text{Kr}_{\text{xs}}$, and $r = 0.86$ when considering individual samples. Note that
896 the GISP2 site is not included in the analysis because it is in Greenland where the elevation- $^{86}\text{Kr}_{\text{xs}}$
897 relationship may be different from Antarctica – it does however fit the Antarctic trend rather well. We
898 further use the simulated WAIS Divide elevation history (Golledge et al., 2014), which simulates an LGM
899 elevation of around 300 m higher than at present at WAIS Divide.

900 **Appendix B: Sub-annual $^{86}\text{Kr}_{\text{xs}}$ variations at DE08-OH**

901 The Law Dome DE08-OH site is a revisit of the DE08 site, drilled in the 2018/2019 Austral summer
902 Antarctic field season. We have samples from two separate cores: (1) thirteen 24-cm-long samples from a
903 10-cm-diameter core going from 97 m to 193 m depth at ~ 8 m sample spacing; and (2) eight 6-cm-long
904 samples from a 24-cm-diameter core going from 97.6 m to 99.8 m depth at 30 cm sample spacing. The
905 purpose of the first set was to determine possible long-term variations in $^{86}\text{Kr}_{\text{xs}}$; the purpose of the second
906 set to assess whether there are sub-annual variations in $^{86}\text{Kr}_{\text{xs}}$ due to the seasonality in firm properties and
907 bubble trapping.

908 Both cores were dry-drilled (i.e., no drill liquid was used). The 10-cm-diameter core used was drilled at the
909 beginning of the field season, the 24-cm-diameter core at the end of the field season. Prior to shipment off
910 the continent, both cores were stored in a chest freezer at Casey Station; due to a miscommunication this
911 freezer was set to -20°C rather than -26°C , yet the ice is believed to have stayed below -18°C .

912 Both DE08-OH cores experienced more gas loss than the original DE08 core that we also sampled (Fig.
913 A1 B). In particular the samples from the 10-cm-diameter core were strongly depleted in $\delta\text{Ar}/\text{N}_2$, with the
914 most extreme gas loss seen for the deepest samples where the ice quality was poorest.

915 Fig. B1 shows the high-resolution sub-annual DE08-OH sampling. The data were corrected for gas loss and
916 thermal fractionation, using a site-mean temperature gradient of $\overline{\Delta T} = -1.6^{\circ}\text{C}$, possibly related to a rectifier
917 effect (Morgan et al. 2022). We find strong (5-fold) variations in $^{86}\text{Kr}_{\text{xs}}$ on sub-annual time scales. With an
918 expected annual layer thickness of around 1.3 m at this depth, it appears as though there may be an annual-
919 scale variation in $^{86}\text{Kr}_{\text{xs}}$; the data set has insufficient length to establish this firmly.

920 We refrain from interpreting the long-term variations in $^{86}\text{Kr}_{\text{xs}}$ in the 10-cm-diameter core for two reasons.
921 First, given the strong sub-annual variations seen in the high-resolution sampling, it is unavoidable that we
922 are aliasing the underlying signal in the core. Second, the 10-cm-diameter core suffers from strong gas loss
923 (depleted $\delta\text{Ar}/\text{N}_2$). We attribute this primarily to the dry drilling and imperfect sample storage conditions.
924 Perhaps the greater stresses during drilling a 10-cm core (compared to the 24-cm diameter core) result in
925 more micro-fractures and gas loss.

926 **Supplement**

927 A data supplement is available with this paper.

928 **Data availability**

929 Data are available here: <https://www.usap-dc.org/view/project/p0010037>, and via the data supplement to
930 this paper.

931 **Author contributions**

932 CB, JS, AJS and EJB designed research; SS, AS, BB, KK, DB, AJS, JDM and IO contributed
933 measurements; KK, DME, NB, RLP, RB, EM-T, PDN, DT, and VVP contributed ice core samples; CB
934 and WHGR analyzed reanalysis data; CB, AJS, and BB performed firm modelling; CB drafted the
935 manuscript with input from all authors.

936 **Competing Interests**

937 The authors declare no competing interests.

938 **Acknowledgements**

939 The idea for the Kr-86 excess proxy came out of discussions at the 2014 WAIS Divide Ice Core Science
940 Meeting held at Scripps Institution of Oceanography in La Jolla, CA. The authors want to thank John
941 Chiang, Justin Wettstein, Zanna Chase, Bob Anderson, Tyler Jones and Eric Steig for useful discussions,
942 data sharing and manuscript feedback, the NSF ice core facility (NSF-ICF, formerly the National Ice Core
943 Laboratory) for curating and distributing ice core samples, the European Centre for Medium-Range
944 Weather Forecasts (ECMWF) for making ERA-Interim reanalysis datasets publicly available, and the US
945 ice drilling program for coordinating ice core drilling in Antarctica. Ice drilling and field support at Law
946 Dome and sample handling in Hobart was provided by the Australian Antarctic Science Program, the
947 Australian Antarctic Division and (at DE08-OH) the U.S. National Science Foundation.

948 **Financial Support**

949 We gratefully acknowledge financial support from the U.S. National Science Foundation (grant numbers
950 ANT-0944343, ANT-1543267, ANT-1543229, ANT-1643716 and ANT-1643669), the New Zealand
951 Ministry of Business, Innovation and Employment (grant numbers RDF-VUW-1103, 15-VUW-131,
952 540GCT32).

- 954 Anderson, R.F., Ali, S., Bradtmiller, L.I., Nielsen, S.H.H., Fleisher, M.Q., Anderson, B.E. and Burckle, L.H. (2009)
 955 Wind-Driven Upwelling in the Southern Ocean and the Deglacial Rise in Atmospheric CO₂. *Science* 323, 1443-
 956 1448.
- 957 Baggenstos, D., Häberli, M., Schmitt, J., Shackleton, S.A., Birner, B., Severinghaus, J.P., Kellerhals, T. and Fischer,
 958 H. (2019) Earth's radiative imbalance from the Last Glacial Maximum to the present. *Proc. Natl. Acad. Sci. U. S.*
 959 *A.*, 201905447.
- 960 Bals-Elsholz, T.M., Atallah, E.H., Bosart, L.F., Wasula, T.A., Cempa, M.J. and Lupo, A.R. (2001) The Wintertime
 961 Southern Hemisphere Split Jet: Structure, Variability, and Evolution. *J. Clim.* 14, 4191-4215.
- 962 Battle, M.O., Severinghaus, J.P., Sofen, E.D., Plotkin, D., Orsi, A.J., Aydin, M., Montzka, S.A., Sowers, T. and Tans,
 963 P.P. (2011) Controls on the movement and composition of firn air at the West Antarctic Ice Sheet Divide. *Atmos.*
 964 *Chem. Phys.* 11, 11007-11021.
- 965 Bender, M., Sowers, T. and Lipenkov, V. (1995) ON THE CONCENTRATIONS OF O-2, N-2, AND AR IN
 966 TRAPPED GASES FROM ICE CORES. *J. Geophys. Res.* 100, 18651-18660.
- 967 Bender, M.L. (2002) Orbital tuning chronology for the Vostok climate record supported by trapped gas composition.
 968 *Earth Planet. Sci. Lett.* 204, 275-289.
- 969 Bereiter, B., Kawamura, K. and Severinghaus, J.P. (2018a) New methods for measuring atmospheric heavy noble gas
 970 isotope and elemental ratios in ice core samples. *Rapid communications in mass spectrometry* 32, 801-814.
- 971 Bereiter, B., Shackleton, S., Baggenstos, D., Kawamura, K. and Severinghaus, J. (2018b) Mean global ocean
 972 temperatures during the last glacial transition. *Nature* 553, 39.
- 973 Birner, B., Buizert, C., Wagner, T.J.W. and Severinghaus, J.P. (2018) The influence of layering and barometric
 974 pumping on firn air transport in a 2-D model. *The Cryosphere* 12, 2021-2037.
- 975 Braconnot, P., Luan, Y., Brewer, S. and Zheng, W. (2012) Impact of Earth's orbit and freshwater fluxes on Holocene
 976 climate mean seasonal cycle and ENSO characteristics. *Clim. Dyn.* 38, 1081-1092.
- 977 Broccoli, A.J., Dahl, K.A. and Stouffer, R.J. (2006) Response of the ITCZ to Northern Hemisphere cooling. *Geophys.*
 978 *Res. Lett.* 33, L01702.
- 979 Buizert, C., Cuffey, K.M., Severinghaus, J.P., Baggenstos, D., Fudge, T.J., Steig, E.J., Markle, B.R., Winstrup, M.,
 980 Rhodes, R.H., Brook, E.J., Sowers, T.A., Clow, G.D., Cheng, H., Edwards, L.R., Sigl, M., McConnell, J.R. and
 981 Taylor, K.C. (2015) The WAIS Divide deep ice core WD2014 chronology - part 1: Methane synchronization (68-
 982 31 ka BP) and the gas age-ice age difference. *Climate of the Past* 11, 153-173.
- 983 Buizert, C. and Severinghaus, J.P. (2016) Dispersion in deep polar firn driven by synoptic-scale surface pressure
 984 variability. *The Cryosphere* 10, 2099-2111.
- 985 Buizert, C., Sigl, M., Severi, M., Markle, B.R., Wettstein, J.J., McConnell, J.R., Pedro, J.B., Sodemann, H., Goto-
 986 Azuma, K., Kawamura, K., Fujita, S., Motoyama, H., Hirabayashi, M., Uemura, R., Stenni, B., Parrenin, F., He,
 987 F., Fudge, T.J. and Steig, E.J. (2018) Abrupt ice-age shifts in southern westerly winds and Antarctic climate forced
 988 from the north. *Nature* 563, 681-685.
- 989 Buizert, C., Sowers, T. and Blunier, T. (2013) Assessment of diffusive isotopic fractionation in polar firn, and
 990 application to ice core trace gas records. *Earth Planet. Sci. Lett.* 361, 110-119.
- 991 Cai, W., Santoso, A., Wang, G., Yeh, S.-W., An, S.-I., Cobb, K.M., Collins, M., Guilyardi, E., Jin, F.-F., Kug, J.-S.,
 992 Lengaigne, M., McPhaden, M.J., Takahashi, K., Timmermann, A., Vecchi, G., Watanabe, M. and Wu, L. (2015)
 993 ENSO and greenhouse warming. *Nature Clim. Change* 5, 849-859.
- 994 Cane, M.A. (2005) The evolution of El Niño, past and future. *Earth Planet. Sci. Lett.* 230, 227-240.
- 995 Ceppi, P., Hwang, Y.-T., Liu, X., Frierson, D.M.W. and Hartmann, D.L. (2013) The relationship between the ITCZ
 996 and the Southern Hemispheric eddy-driven jet. *J. Geophys. Res.* 118, 5136-5146.
- 997 Chase, Z., Anderson, R.F., Fleisher, M.Q. and Kubik, P.W. (2003) Accumulation of biogenic and lithogenic material
 998 in the Pacific sector of the Southern Ocean during the past 40,000 years. *Deep Sea Research Part II: Topical Studies*
 999 *in Oceanography* 50, 799-832.
- 1000 Cheng, H., Edwards, R.L., Sinha, A., Spötl, C., Yi, L., Chen, S., Kelly, M., Kathayat, G., Wang, X., Li, X., Kong, X.,
 1001 Wang, Y., Ning, Y. and Zhang, H. (2016) The Asian monsoon over the past 640,000 years and ice age terminations.
 1002 *Nature* 534, 640-646.
- 1003 Chiang, J.C. and Friedman, A.R. (2012) Extratropical cooling, interhemispheric thermal gradients, and tropical
 1004 climate change. *Annu. Rev. Earth Planet. Sci.* 40, 383-412.
- 1005 Chiang, J.C.H. and Bitz, C.M. (2005) Influence of high latitude ice cover on the marine Intertropical Convergence
 1006 Zone. *Clim. Dyn.* 25, 477-496.

1007 Chiang, J.C.H., Lee, S.-Y., Putnam, A.E. and Wang, X. (2014) South Pacific Split Jet, ITCZ shifts, and atmospheric
1008 North–South linkages during abrupt climate changes of the last glacial period. *Earth Planet. Sci. Lett.* 406, 233-
1009 246.

1010 Clement, A.C., Seager, R. and Cane, M.A. (2000) Suppression of El Niño during the Mid-Holocene by changes in the
1011 Earth's orbit. *Paleoceanography* 15, 731-737.

1012 Cobb, K.M., Westphal, N., Sayani, H.R., Watson, J.T., Di Lorenzo, E., Cheng, H., Edwards, R.L. and Charles, C.D.
1013 (2013) Highly Variable El Niño–Southern Oscillation Throughout the Holocene. *Science* 339, 67-70.

1014 Conroy, J.L., Overpeck, J.T., Cole, J.E., Shanahan, T.M. and Steinitz-Kannan, M. (2008) Holocene changes in eastern
1015 tropical Pacific climate inferred from a Galápagos lake sediment record. *Quat. Sci. Rev.* 27, 1166-1180.

1016 Cruz, F.W., Burns, S.J., Karmann, I., Sharp, W.D., Vuille, M., Cardoso, A.O., Ferrari, J.A., Dias, P.L.S. and Viana,
1017 O. (2005) Insolation-driven changes in atmospheric circulation over the past 116,000 years in subtropical Brazil.
1018 *Nature* 434, 63-66.

1019 Dee, D.P., Uppala, S.M., Simmons, A.J., Berrisford, P., Poli, P., Kobayashi, S., Andrae, U., Balmaseda, M.A.,
1020 Balsamo, G., Bauer, P., Bechtold, P., Beljaars, A.C.M., van de Berg, L., Bidlot, J., Bormann, N., Delsol, C.,
1021 Dragani, R., Fuentes, M., Geer, A.J., Haimberger, L., Healy, S.B., Hersbach, H., Hólm, E.V., Isaksen, I., Kållberg,
1022 P., Köhler, M., Matricardi, M., McNally, A.P., Monge-Sanz, B.M., Morcrette, J.J., Park, B.K., Peubey, C., de
1023 Rosnay, P., Tavolato, C., Thépaut, J.N. and Vitart, F. (2011) The ERA-Interim reanalysis: configuration and
1024 performance of the data assimilation system. *Quarterly Journal of the Royal Meteorological Society* 137, 553-597.

1025 Driscoll, R., Elliot, M., Russon, T., Welsh, K., Yokoyama, Y. and Tudhope, A. (2014) ENSO reconstructions over the
1026 past 60 ka using giant clams (*Tridacna* sp.) from Papua New Guinea. *Geophys. Res. Lett.* 41, 6819-6825.

1027 Dykoski, C.A., Edwards, R.L., Cheng, H., Yuan, D.X., Cai, Y.J., Zhang, M.L., Lin, Y.S., Qing, J.M., An, Z.S. and
1028 Revenaugh, J. (2005) A high-resolution, absolute-dated Holocene and deglacial Asian monsoon record from
1029 Dongge Cave, China. *Earth Planet. Sci. Lett.* 233, 71-86.

1030 Emile-Geay, J., Cobb, K.M., Carré, M., Braconnot, P., Leloup, J., Zhou, Y., Harrison, S.P., Corrège, T., McGregor,
1031 H.V., Collins, M., Driscoll, R., Elliot, M., Schneider, B. and Tudhope, A. (2015) Links between tropical Pacific
1032 seasonal, interannual and orbital variability during the Holocene. *Nat. Geosci.* 9, 168.

1033 Etheridge, D.M., Pearman, G.I. and Fraser, P.J. (1992) CHANGES IN TROPOSPHERIC METHANE BETWEEN
1034 1841 AND 1978 FROM A HIGH ACCUMULATION-RATE ANTARCTIC ICE CORE. *Tellus* 44, 282-294.

1035 Fahnestock, M.A., Scambos, T.A., Shuman, C.A., Arthern, R.J., Winebrenner, D.P. and Kwok, R. (2000) Snow
1036 megadune fields on the East Antarctic Plateau: Extreme atmosphere-ice interaction. *Geophys. Res. Lett.* 27, 3719-
1037 3722.

1038 Fowler, A.M., Boswijk, G., Lorrey, A.M., Gergis, J., Pirie, M., McCloskey, S.P.J., Palmer, J.G. and Wunder, J. (2012)
1039 Multi-centennial tree-ring record of ENSO-related activity in New Zealand. *Nature Climate Change* 2, 172.

1040 Fujita, S., Okuyama, J., Hori, A. and Hondoh, T. (2009) Metamorphism of stratified firn at Dome Fuji, Antarctica: A
1041 mechanism for local insolation modulation of gas transport conditions during bubble close off. *J. Geophys. Res.*
1042 114.

1043 Gergis, J.L. and Fowler, A.M. (2009) A history of ENSO events since A.D. 1525: implications for future climate
1044 change. *Clim. Change* 92, 343-387.

1045 Golledge, N.R., Meniel, L., Carter, L., Fogwill, C.J., England, M.H., Cortese, G. and Levy, R.H. (2014) Antarctic
1046 contribution to meltwater pulse 1A from reduced Southern Ocean overturning. *Nat Comm.* 5, 5107.

1047 Grachev, A.M. and Severinghaus, J.P. (2003a) Determining the thermal diffusion factor for Ar-40/Ar-36 in air to aid
1048 paleoreconstruction of abrupt climate change. *J. Phys. Chem. A* 107, 4636-4642.

1049 Grachev, A.M. and Severinghaus, J.P. (2003b) Laboratory determination of thermal diffusion constants for N-
1050 29(2)/N-28(2) in air at temperatures from -60 to 0 degrees C for reconstruction of magnitudes of abrupt climate
1051 changes using the ice core fossil-air paleothermometer. *Geochim. Cosmochim. Acta* 67, 345-360.

1052 Grootes, P.M., Stuiver, M., White, J.W.C., Johnsen, S. and Jouzel, J. (1993) Comparison of oxygen isotope records
1053 from the GISP2 and GRIP Greenland ice cores. *Nature* 366, 552-554.

1054 Headly, M.A. and Severinghaus, J.P. (2007) A method to measure Kr/N-2 ratios in air bubbles trapped in ice cores
1055 and its application in reconstructing past mean ocean temperature. *J. Geophys. Res.* 112, 12.

1056 Herron, M.M. and Langway, C.C. (1980) Firn densification: An empirical model. *J. Glaciol.* 25, 373-385.

1057 Huang, B., Banzon, V.F., Freeman, E., Lawrimore, J., Liu, W., Peterson, T.C., Smith, T.M., Thorne, P.W., Woodruff,
1058 S.D. and Zhang, H.-M. (2014) Extended Reconstructed Sea Surface Temperature Version 4 (ERSST.v4). Part I:
1059 Upgrades and Intercomparisons. *J. Clim.* 28, 911-930.

1060 Huber, C., Beyerle, U., Leuenberger, M., Schwander, J., Kipfer, R., Spahni, R., Severinghaus, J.P. and Weiler, K.
1061 (2006) Evidence for molecular size dependent gas fractionation in firn air derived from noble gases, oxygen, and
1062 nitrogen measurements. *Earth Planet. Sci. Lett.* 243, 61-73.

1063 Ikeda-Fukazawa, T., Fukumizu, K., Kawamura, K., Aoki, S., Nakazawa, T. and Hondoh, T. (2005) Effects of
1064 molecular diffusion on trapped gas composition in polar ice cores. *Earth Planet. Sci. Lett.* 229, 183-192.

1065 Kanner, L.C., Burns, S.J., Cheng, H. and Edwards, R.L. (2012) High-Latitude Forcing of the South American Summer
1066 Monsoon During the Last Glacial. *Science* 335, 570-573

1067 Kawamura, K., Severinghaus, J.P., Albert, M.R., Courville, Z.R., Fahnestock, M.A., Scambos, T., Shields, E. and
1068 Shuman, C.A. (2013) Kinetic fractionation of gases by deep air convection in polar firn. *Atmos. Chem. Phys.* 13,
1069 11141-11155.

1070 Kawamura, K., Severinghaus, J.P., Ishidoya, S., Sugawara, S., Hashida, G., Motoyama, H., Fujii, Y., Aoki, S. and
1071 Nakazawa, T. (2006) Convective mixing of air in firn at four polar sites. *Earth Planet. Sci. Lett.* 244, 672-682.

1072 Kobashi, T., Severinghaus, J.P. and Barnola, J.M. (2008a) 4 +/- 1.5 degrees C abrupt warming 11,270 yr ago identified
1073 from trapped air in Greenland ice. *Earth Planet. Sci. Lett.* 268, 397-407.

1074 Kobashi, T., Severinghaus, J.P. and Kawamura, K. (2008b) Argon and nitrogen isotopes of trapped air in the GISP2
1075 ice core during the Holocene epoch (0-11,500 B.P.): Methodology and implications for gas loss processes.
1076 *Geochim. Cosmochim. Acta* 72, 4675-4686.

1077 Kohfeld, K.E., Graham, R.M., de Boer, A.M., Sime, L.C., Wolff, E.W., Le Quéré, C. and Bopp, L. (2013) Southern
1078 Hemisphere westerly wind changes during the Last Glacial Maximum: paleo-data synthesis. *Quat. Sci. Rev.* 68,
1079 76-95.

1080 Koutavas, A., deMenocal, P.B., Olive, G.C. and Lynch-Stieglitz, J. (2006) Mid-Holocene El Niño–Southern
1081 Oscillation (ENSO) attenuation revealed by individual foraminifera in eastern tropical Pacific sediments. *Geology*
1082 34, 993-996.

1083 Koutavas, A., Lynch-Stieglitz, J., Marchitto, T.M. and Sachs, J.P. (2002) El Niño-Like Pattern in Ice Age Tropical
1084 Pacific Sea Surface Temperature. *Science* 297, 226-230.

1085 Lamy, F., Chiang, J.C.H., Martínez-Méndez, G., Thierens, M., Arz, H.W., Bosmans, J., Hebbeln, D., Lambert, F.,
1086 Lembke-Jene, L. and Stuut, J.-B. (2019) Precession modulation of the South Pacific westerly wind belt over the
1087 past million years. *Proc. Natl. Acad. Sci. U. S. A.*, 201905847.

1088 Lee, S. and Kim, H.-k. (2003) The Dynamical Relationship between Subtropical and Eddy-Driven Jets. *Journal of the*
1089 *Atmospheric Sciences* 60, 1490-1503.

1090 Lee, S.Y., Chiang, J.C., Matsumoto, K. and Tokos, K.S. (2011) Southern Ocean wind response to North Atlantic
1091 cooling and the rise in atmospheric CO₂: Modeling perspective and paleoceanographic implications.
1092 *Paleoceanography* 26.

1093 Liu, Z., Kutzbach, J. and Wu, L. (2000) Modeling climate shift of El Niño variability in the Holocene. *Geophys. Res.*
1094 *Lett.* 27, 2265-2268.

1095 Liu, Z., Lu, Z., Wen, X., Otto-Bliessner, B.L., Timmermann, A. and Cobb, K.M. (2014) Evolution and forcing
1096 mechanisms of El Niño over the past 21,000 years. *Nature* 515, 550-553.

1097 Lynch-Stieglitz, J. (2017) The Atlantic Meridional Overturning Circulation and Abrupt Climate Change. *Annual*
1098 *Review of Marine Science* 9, 83-104.

1099 Mantua, N.J. and Hare, S.R. (2002) The Pacific Decadal Oscillation. *Journal of Oceanography* 58, 35-44.

1100 Marcott, S.A., Shakun, J.D., Clark, P.U. and Mix, A.C. (2013) A Reconstruction of Regional and Global Temperature
1101 for the Past 11,300 Years. *Science* 339, 1198-1201.

1102 Marino, G., Zahn, R., Ziegler, M., Purcell, C., Knorr, G., Hall, I.R., Ziveri, P. and Elderfield, H. (2013) Agulhas salt-
1103 leakage oscillations during abrupt climate changes of the Late Pleistocene. *Paleoceanography* 28, 599-606.

1104 Markle, B.R., Steig, E.J., Buizert, C., Schoenemann, S.W., Bitz, C.M., Fudge, T.J., Pedro, J.B., Ding, Q., Jones, T.R.,
1105 White, J.W.C. and Sowers, T. (2017) Global atmospheric teleconnections during Dansgaard-Oeschger events.
1106 *Nature Geosci* 10, 36-40.

1107 Marshall, J. and Speer, K. (2012) Closure of the meridional overturning circulation through Southern Ocean
1108 upwelling. *Nature Geosci* 5, 171-180.

1109 McGee, D., Donohoe, A., Marshall, J. and Ferreira, D. (2014) Changes in ITCZ location and cross-equatorial heat
1110 transport at the Last Glacial Maximum, Heinrich Stadial 1, and the mid-Holocene. *Earth Planet. Sci. Lett.* 390, 69-
1111 79.

1112 Merkel, U., Prange, M. and Schulz, M. (2010) ENSO variability and teleconnections during glacial climates. *Quat.*
1113 *Sci. Rev.* 29, 86-100.

1114 Mo, K.C. and Paegle, J.N. (2001) The Pacific–South American modes and their downstream effects. *International*
1115 *Journal of Climatology* 21, 1211-1229.

1116 Moy, C.M., Seltzer, G.O., Rodbell, D.T. and Anderson, D.M. (2002) Variability of El Niño/Southern Oscillation
1117 activity at millennial timescales during the Holocene epoch. *Nature* 420, 162.

1118 Nakamura, H. and Shimpo, A. (2004) Seasonal Variations in the Southern Hemisphere Storm Tracks and Jet Streams
1119 as Revealed in a Reanalysis Dataset. *J. Clim.* 17, 1828-1844.

1120 Orsi, A.J., Kawamura, K., Fegyveresi, J.M., Headly, M.A., Alley, R.B. and Severinghaus, J.P. (2015) Differentiating
1121 bubble-free layers from melt layers in ice cores using noble gases. *J. Glaciol.* 61, 585-594.

1122 Oyabu, I., Kawamura, K., Uchida, T., Fujita, S., Kitamura, K., Hirabayashi, M., Aoki, S., Morimoto, S., Nakazawa,
1123 T., Severinghaus, J.P. and Morgan, J.D. (2021) Fractionation of O₂N₂ and ArN₂ in the Antarctic ice sheet during
1124 bubble formation and bubble-clathrate hydrate transition from precise gas measurements of the Dome Fuji ice
1125 core. *The Cryosphere* 15, 5529-5555.

1126 Parkinson, C.L. and Cavalieri, D.J. (2012) Antarctic sea ice variability and trends, 1979–2010. *The Cryosphere*
1127 6, 871-880.

1128 Pedro, J.B., Jochum, M., Buizert, C., He, F., Barker, S. and Rasmussen, S.O. (2018) Beyond the bipolar seesaw:
1129 Toward a process understanding of interhemispheric coupling. *Quat. Sci. Rev.* 192, 27-46.

1130 Peterson, L.C., Haug, G.H., Hughen, K.A. and Röhl, U. (2000) Rapid Changes in the Hydrologic Cycle of the Tropical
1131 Atlantic During the Last Glacial. *Science* 290, 1947-1951.

1132 Rahmstorf, S. (2002) Ocean circulation and climate during the past 120,000 years. *Nature* 419, 207-214.

1133 Raynaud, D., Lipenkov, V., Lemieux-Dudon, B., Duval, P., Loutre, M.F. and Lhomme, N. (2007) The local insolation
1134 signature of air content in Antarctic ice. A new step toward an absolute dating of ice records. *Earth Planet. Sci.*
1135 *Lett.* 261, 337-349.

1136 Rein, B., Lückge, A., Reinhardt, L., Sirocko, F., Wolf, A. and Dullo, W.-C. (2005) El Niño variability off Peru during
1137 the last 20,000 years. *Paleoceanography* 20.

1138 Rhodes, R.H., Fain, X., Brook, E.J., McConnell, J.R., Maselli, O.J., Sigl, M., Edwards, J., Buizert, C., Blunier, T.,
1139 Chappellaz, J. and Freitag, J. (2016) Local artifacts in ice core methane records caused by layered bubble trapping
1140 and in situ production: a multi-site investigation. *Clim. Past* 12, 1061-1077.

1141 Riedinger, M.A., Steinitz-Kannan, M., Last, W.M. and Brenner, M. (2002) A ~6100 14C yr record of El Niño activity
1142 from the Galápagos Islands. *Journal of Paleolimnology* 27, 1-7.

1143 Rind, D., Russell, G., Schmidt, G., Sheth, S., Collins, D., Demenocal, P. and Teller, J. (2001) Effects of glacial
1144 meltwater in the GISS coupled atmosphere-ocean model: 2. A bipolar seesaw in Atlantic Deep Water production.
1145 *Journal of Geophysical Research: Atmospheres* (1984–2012) 106, 27355-27365.

1146 Rojas, M., Moreno, P., Kageyama, M., Crucifix, M., Hewitt, C., Abe-Ouchi, A., Ohgaito, R., Brady, E.C. and Hope,
1147 P. (2009) The Southern Westerlies during the last glacial maximum in PMIP2 simulations. *Clim. Dyn.* 32, 525-
1148 548.

1149 Rommelaere, V., Arnaud, L., and Barnola, J.M. (1997) Reconstructing recent atmospheric trace gas concentrations
1150 from polar firn and bubbly ice data by inverse methods. *J. Geophys. Res.* 102, 30069-30083.

1151 Russell, J.L., Dixon, K.W., Gnanadesikan, A., Stouffer, R.J. and Toggweiler, J.R. (2006) The Southern Hemisphere
1152 Westerlies in a Warming World: Propping Open the Door to the Deep Ocean. *J. Clim.* 19, 6382-6390.

1153 Sadekov, A.Y., Ganeshram, R., Pichevin, L., Berdin, R., McClymont, E., Elderfield, H. and Tudhope, A.W. (2013)
1154 Palaeoclimate reconstructions reveal a strong link between El Niño-Southern Oscillation and Tropical Pacific mean
1155 state. *Nature Communications* 4, 2692.

1156 Salau, O., Schneider, B., Park, W., Khon, V. and Latif, M. (2012) Modeling the ENSO impact of orbitally induced
1157 mean state climate changes. *J. Geophys. Res.* 117.

1158 Schaller, C.F., Freitag, J. and Eisen, O. (2017) Critical porosity of gas enclosure in polar firn independent of climate.
1159 *Clim. Past* 13, 1685-1693.

1160 Schneider, T., Bischoff, T. and Haug, G.H. (2014) Migrations and dynamics of the intertropical convergence zone.
1161 *Nature* 513, 45-53.

1162 Schwander, J. (1989) The transformation of snow to ice and the occlusion of gases in: Oescher, H., Langway, C.C.
1163 (Eds.), *The Environmental record in glaciers and ice sheets*. John Wiley, New York, pp. 53-67.

1164 Schwander, J., Barnola, J.M., Andrie, C., Leuenberger, M., Ludin, A., Raynaud, D. and Stauffer, B. (1993) THE AGE
1165 OF THE AIR IN THE FIRN AND THE ICE AT SUMMIT, GREENLAND. *J. Geophys. Res.* 98, 2831-2838.

1166 Schwander, J., Stauffer, B. and Sigg, A. (1988) Air mixing in firn and the age of the air at pore close-off, *Annals of*
1167 *Glaciology*, pp. 141-145.

1168 Severinghaus, J.P., Albert, M.R., Courville, Z.R., Fahnestock, M.A., Kawamura, K., Montzka, S.A., Muhle, J.,
1169 Scambos, T.A., Shields, E., Shuman, C.A., Suwa, M., Tans, P. and Weiss, R.F. (2010) Deep air convection in the
1170 firn at a zero-accumulation site, central Antarctica. *Earth Planet. Sci. Lett.* 293, 359-367.

1171 Severinghaus, J.P. and Battle, M.O. (2006) Fractionation of gases in polar ice during bubble close-off: New constraints
1172 from firn air Ne, Kr and Xe observations. *Earth Planet. Sci. Lett.* 244, 474-500.

1173 Severinghaus, J.P., Beaudette, R., Headly, M.A., Taylor, K. and Brook, E.J. (2009) Oxygen-18 of O₂ Records the
1174 Impact of Abrupt Climate Change on the Terrestrial Biosphere. *Science* 324, 1431-1434.

1175 Severinghaus, J.P., Grachev, A., Luz, B. and Caillon, N. (2003) A method for precise measurement of argon 40/36
1176 and krypton/argon ratios in trapped air in polar ice with applications to past firn thickness and abrupt climate
1177 change in Greenland and at Siple Dome, Antarctica. *Geochim. Cosmochim. Acta* 67, 325-343.

1178 Severinghaus, J.P., Sowers, T., Brook, E.J., Alley, R.B. and Bender, M.L. (1998) Timing of abrupt climate change at
1179 the end of the Younger Dryas interval from thermally fractionated gases in polar ice. *Nature* 391, 141-146.

1180 Shakun, J.D., Clark, P.U., He, F., Marcott, S.A., Mix, A.C., Liu, Z., Otto-Bliesner, B., Schmittner, A. and Bard, E.
1181 (2012) Global warming preceded by increasing carbon dioxide concentrations during the last deglaciation. *Nature*
1182 484, 49-54.

1183 Sime, L.C., Kohfeld, K.E., Le Quéré, C., Wolff, E.W., de Boer, A.M., Graham, R.M. and Bopp, L. (2013) Southern
1184 Hemisphere westerly wind changes during the Last Glacial Maximum: model-data comparison. *Quat. Sci. Rev.*
1185 64, 104-120.

1186 Simpson, I.R., Hitchcock, P., Shepherd, T.G. and Scinocca, J.F. (2011) Stratospheric variability and tropospheric
1187 annular-mode timescales. *Geophys. Res. Lett.* 38.

1188 Sowers, T., Bender, M., Raynaud, D. and Korotkevich, Y.S. (1992) $\delta^{15}\text{N}$ of N₂ in air trapped in polar ice: A tracer
1189 of gas transport in the firn and a possible constraint on ice age-gas age differences. *J. Geophys. Res.* 97, 15683-
1190 15697.

1191 Stott, L., Poulsen, C., Lund, S. and Thunell, R. (2002) Super ENSO and Global Climate Oscillations at Millennial
1192 Time Scales. *Science* 297, 222-226.

1193 Studer, A.S., Sigman, D.M., Martínez-García, A., Benz, V., Winckler, G., Kuhn, G., Esper, O., Lamy, F., Jaccard,
1194 S.L., Wacker, L., Oleynik, S., Gersonde, R. and Haug, G.H. (2015) Antarctic Zone nutrient conditions during the
1195 last two glacial cycles. *Paleoceanography* 30, 2014PA002745.

1196 Studer, A.S., Sigman, D.M., Martínez-García, A., Thöle, L.M., Michel, E., Jaccard, S.L., Lippold, J.A., Mazaud, A.,
1197 Wang, X.T., Robinson, L.F., Adkins, J.F. and Haug, G.H. (2018) Increased nutrient supply to the Southern Ocean
1198 during the Holocene and its implications for the pre-industrial atmospheric CO₂ rise. *Nat. Geosci.* 11, 756-760.

1199 Thomas, E.R., Marshall, G.J. and McConnell, J.R. (2008) A doubling in snow accumulation in the western Antarctic
1200 Peninsula since 1850. *Geophys. Res. Lett.* 35.

1201 Thompson, D.W.J. and Wallace, J.M. (2000) Annular Modes in the Extratropical Circulation. Part I: Month-to-Month
1202 Variability*. *J. Clim.* 13, 1000-1016.

1203 Thompson, L.G., Mosley-Thompson, E., Davis, M.E., Zagorodnov, V.S., Howat, I.M., Mikhailenko, V.N. and Lin, P.-
1204 N. (2013) Annually Resolved Ice Core Records of Tropical Climate Variability over the Past ~1800 Years. *Science*
1205 340, 945-950.

1206 Timmermann, A., Okumura, Y., An, S.I., Clement, A., Dong, B., Guilyardi, E., Hu, A., Jungclaus, J.H., Renold, M.,
1207 Stocker, T.F., Stouffer, R.J., Sutton, R., Xie, S.P. and Yin, J. (2007) The Influence of a Weakening of the Atlantic
1208 Meridional Overturning Circulation on ENSO. *J. Clim.* 20, 4899-4919.

1209 Toggweiler, J.R., Russell, J.L. and Carson, S.R. (2006) Midlatitude westerlies, atmospheric CO₂, and climate change
1210 during the ice ages. *Paleoceanography* 21, PA2005.

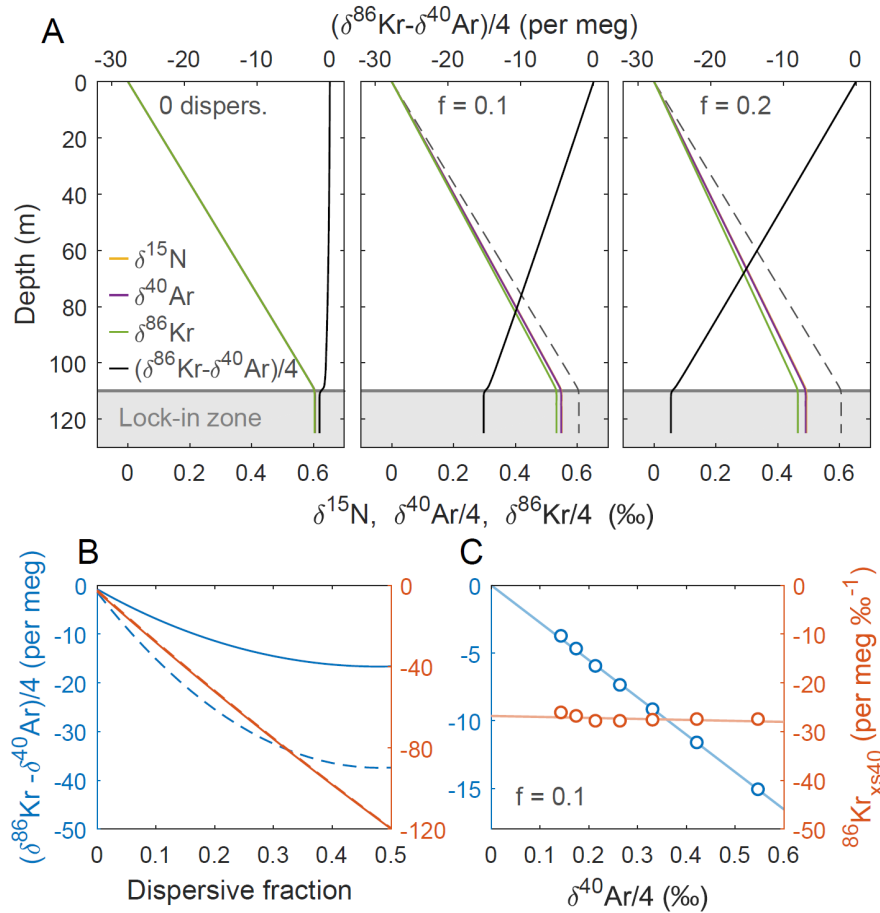
1211 Trenberth, K.E. (1991) Storm Tracks in the Southern Hemisphere. *Journal of the Atmospheric Sciences* 48, 2159-
1212 2178.

1213 Tudhope, A.W., Chilcott, C.P., McCulloch, M.T., Cook, E.R., Chappell, J., Ellam, R.M., Lea, D.W., Lough, J.M. and
1214 Shimmield, G.B. (2001) Variability in the El Niño-Southern Oscillation through a glacial-interglacial cycle.
1215 *Science* 291, 1511-1517.

1216 Wang, X., Auler, A.S., Edwards, R.L., Cheng, H., Ito, E., Wang, Y., Kong, X. and Solheid, M. (2007) Millennial-
1217 scale precipitation changes in southern Brazil over the past 90,000 years. *Geophys. Res. Lett.* 34.

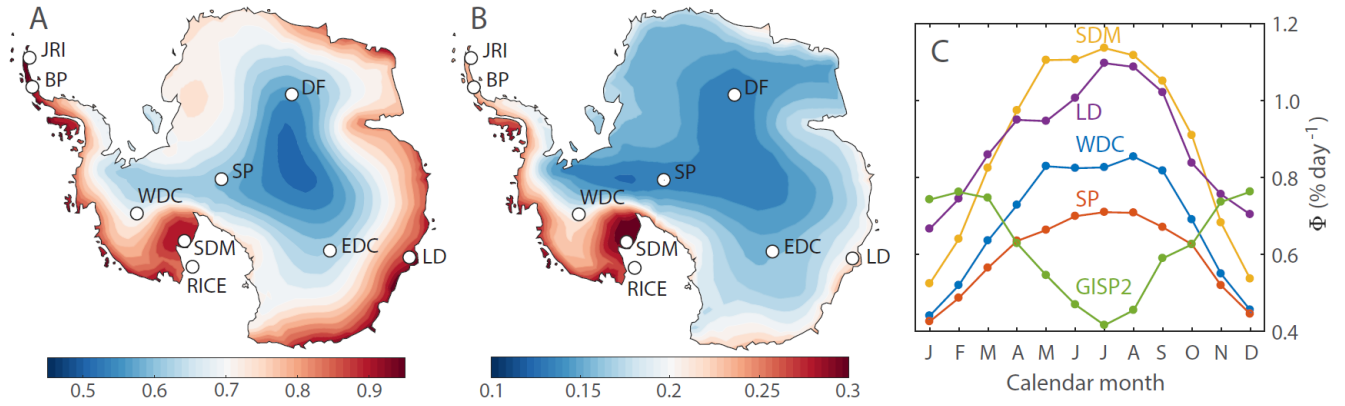
1218 Wang, Y.J., Cheng, H., Edwards, R.L., An, Z.S., Wu, J.Y., Shen, C.C. and Dorale, J.A. (2001) A High-Resolution
1219 Absolute-Dated Late Pleistocene Monsoon Record from Hulu Cave, China. *Science* 294, 2345-2348.

1220 Zheng, W., Braconnot, P., Guilyardi, E., Merkel, U. and Yu, Y. (2008) ENSO at 6ka and 21ka from ocean-atmosphere
1221 coupled model simulations. *Clim. Dyn.* 30, 745-762.



1222

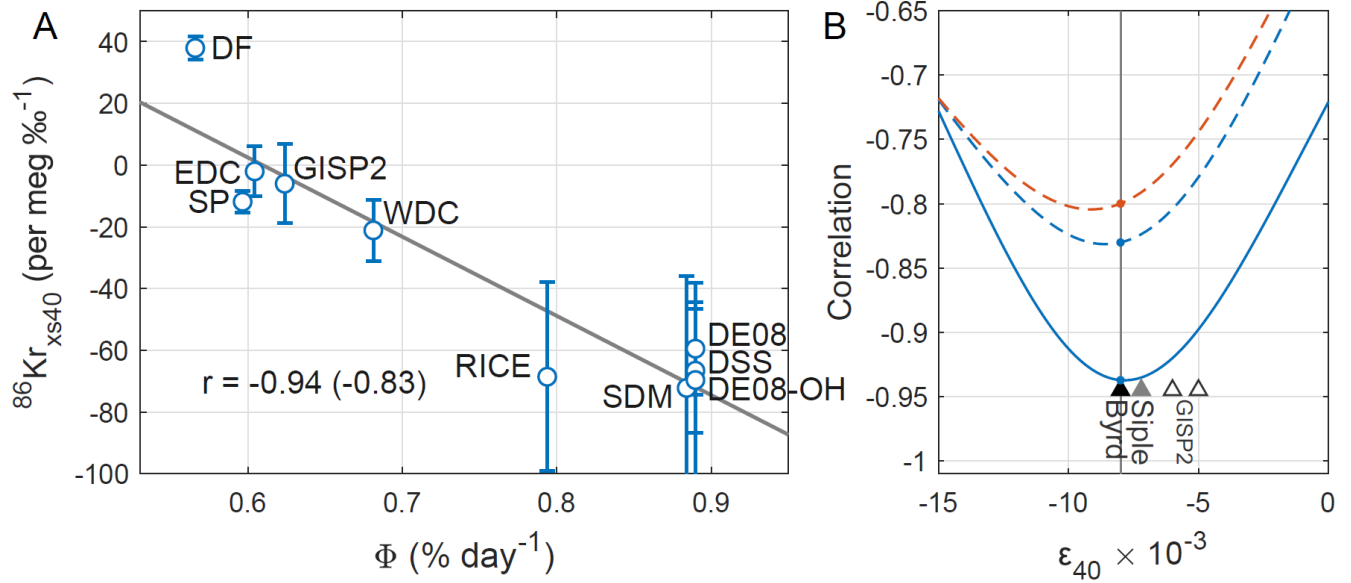
1223 **Figure 1.** Idealized firn air transport model experiments of $^{86}\text{Kr}_{\text{xs}}$. Firn density is calculated using (Herron
 1224 and Langway, 1980), and the diffusivity using (Schwander, 1989). **A** Simulations using a fraction of
 1225 dispersive mixing of $f=0$ (left), $f=0.1$ (middle) and $f=0.2$ (right) for a hypothetical site with accumulation
 1226 rate of $A = 2 \text{ cm a}^{-1}$ ice equivalent and mean annual temperature $T = -60^\circ\text{C}$. At dispersive fraction f , effective
 1227 molecular diffusivity of all gases is multiplied by $(1-f)$ and dispersive mixing for all gases is set equal to f
 1228 times the effective molecular diffusivity of CO_2 . **B** Isotopic disequilibrium as a function of dispersive
 1229 mixing intensity at two different firn thicknesses of around 100 m (dashed, $A = 2 \text{ cm a}^{-1}$ and $T = -60^\circ\text{C}$) and
 1230 50 m (solid, $A = 2 \text{ cm a}^{-1}$ and $T = -43^\circ\text{C}$). We compare isotopic disequilibrium without (blue, left axis) and
 1231 with (orange, right axis) normalization. **C** Simulations at 10 % dispersive mixing, where each dot represents
 1232 different climatic conditions. Accumulation rate is $A = 2 \text{ cm a}^{-1}$ ice equivalent and mean annual temperature
 1233 is changed from -60°C to -30°C in steps of 5°C .



1234

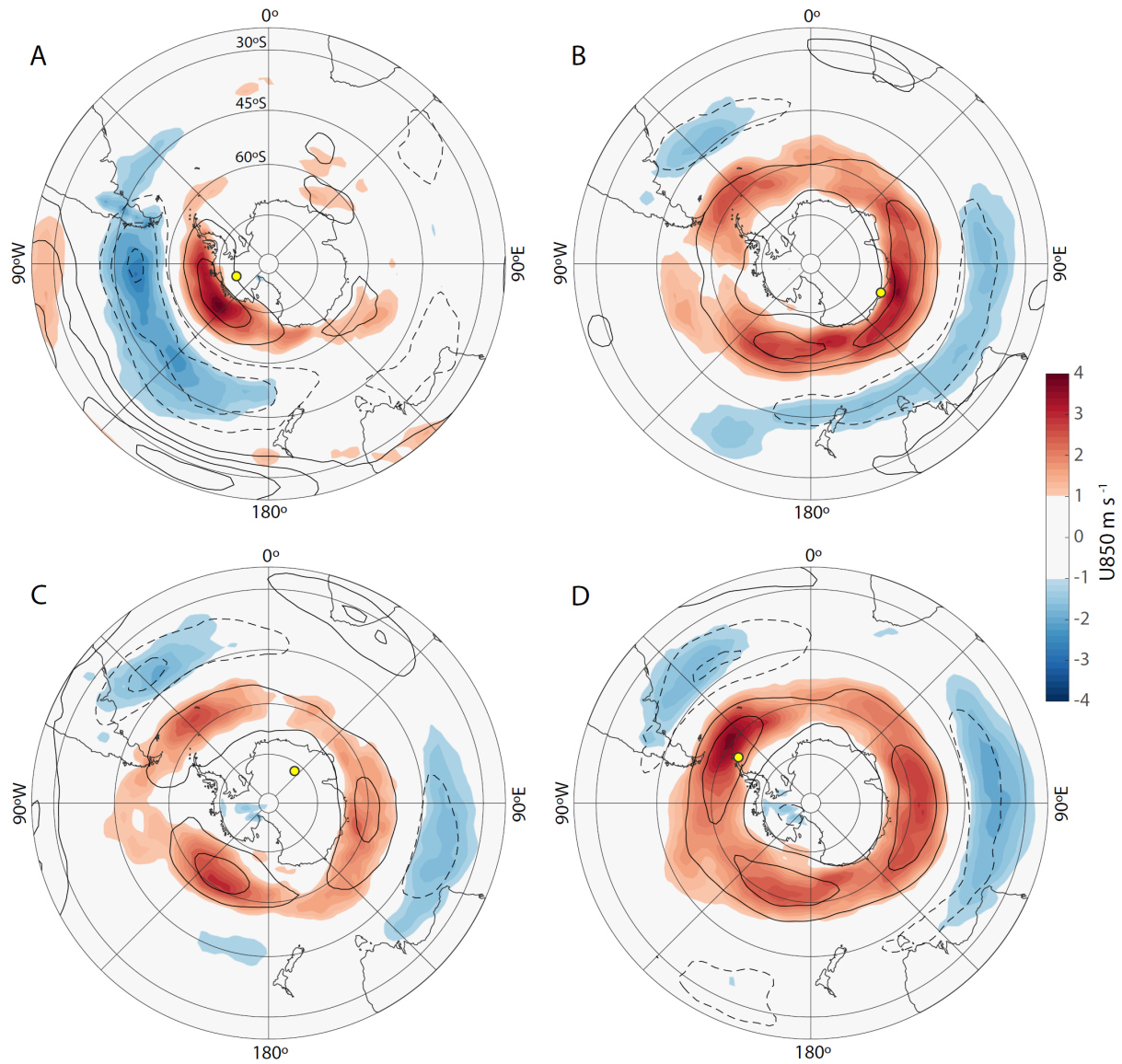
1235

1236 **Figure 2.** Calibrating Kr-86 excess. **A** Annual-mean Φ in Antarctica over 1979-2017, in units of $\% \text{ day}^{-1}$.
 1237 **B** Interannual variability (1σ standard deviation) of annual-mean Φ over 1979-2017, in units of $\% \text{ day}^{-1}$. **C**
 1238 Annual cycle in Φ for 1979-2017 for the indicated sites.



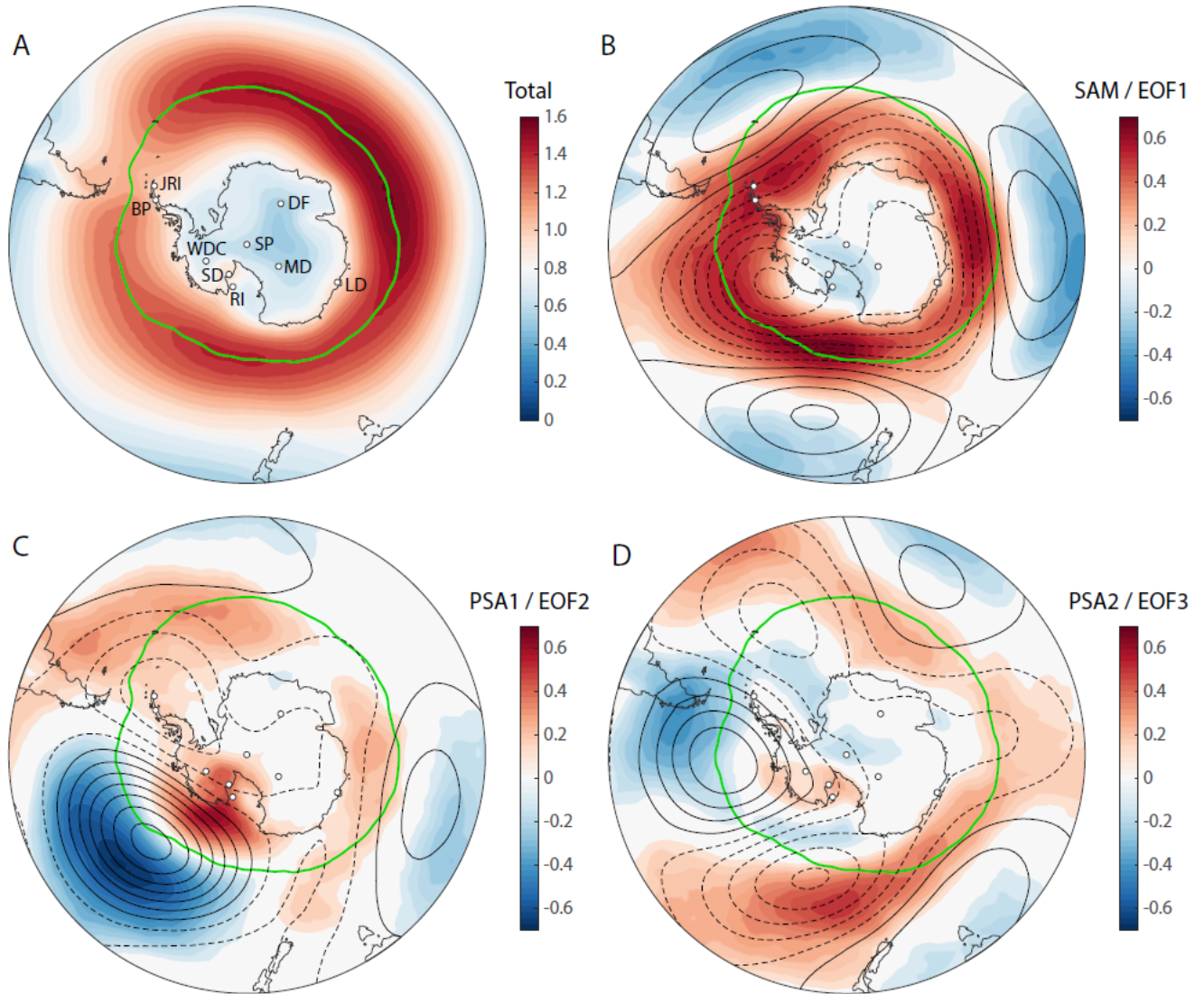
1239

1240 **Figure 3.** Calibrating Kr-86 excess. **A** $^{86}\text{Kr}_{\text{xs}}$ as a function of Φ for the calibration data set. Circles give the
 1241 site mean, and the error bars denote the $\pm 1\sigma$ standard deviation between samples (uncertainty in corrections
 1242 and measurements not included). The number of samples at each site is given in Table 1. Pearson correlation
 1243 coefficient is $r = -0.94$ when considering site data means and $r = -0.83$ when considering all individual
 1244 samples. Data are corrected for gas loss using $\epsilon_{40} = -0.008$ (Appendix A1), and corrected for thermal
 1245 fractionation using site-mean ^{15}N excess (Appendix A2). The calibration curve for $^{86}\text{Kr}_{\text{xs}15}$ is identical in
 1246 this case, with slightly larger errorbars. **B** Correlation of the calibration curve as a function of the gas loss
 1247 correction scaling parameter ϵ_{40} . The solid line gives the correlation for both site-mean $^{86}\text{Kr}_{\text{xs}15}$ and $^{86}\text{Kr}_{\text{xs}40}$
 1248 (identical); the dashed lines the correlation using individual samples for $^{86}\text{Kr}_{\text{xs}40}$ (blue) and $^{86}\text{Kr}_{\text{xs}15}$ (orange).
 1249 Triangles denote the ϵ_{40} estimate from the Byrd, Siple and GISP2 ice cores (Fig. A2; Kobashi et al., 2008a;
 1250 Severinghaus et al., 2003).



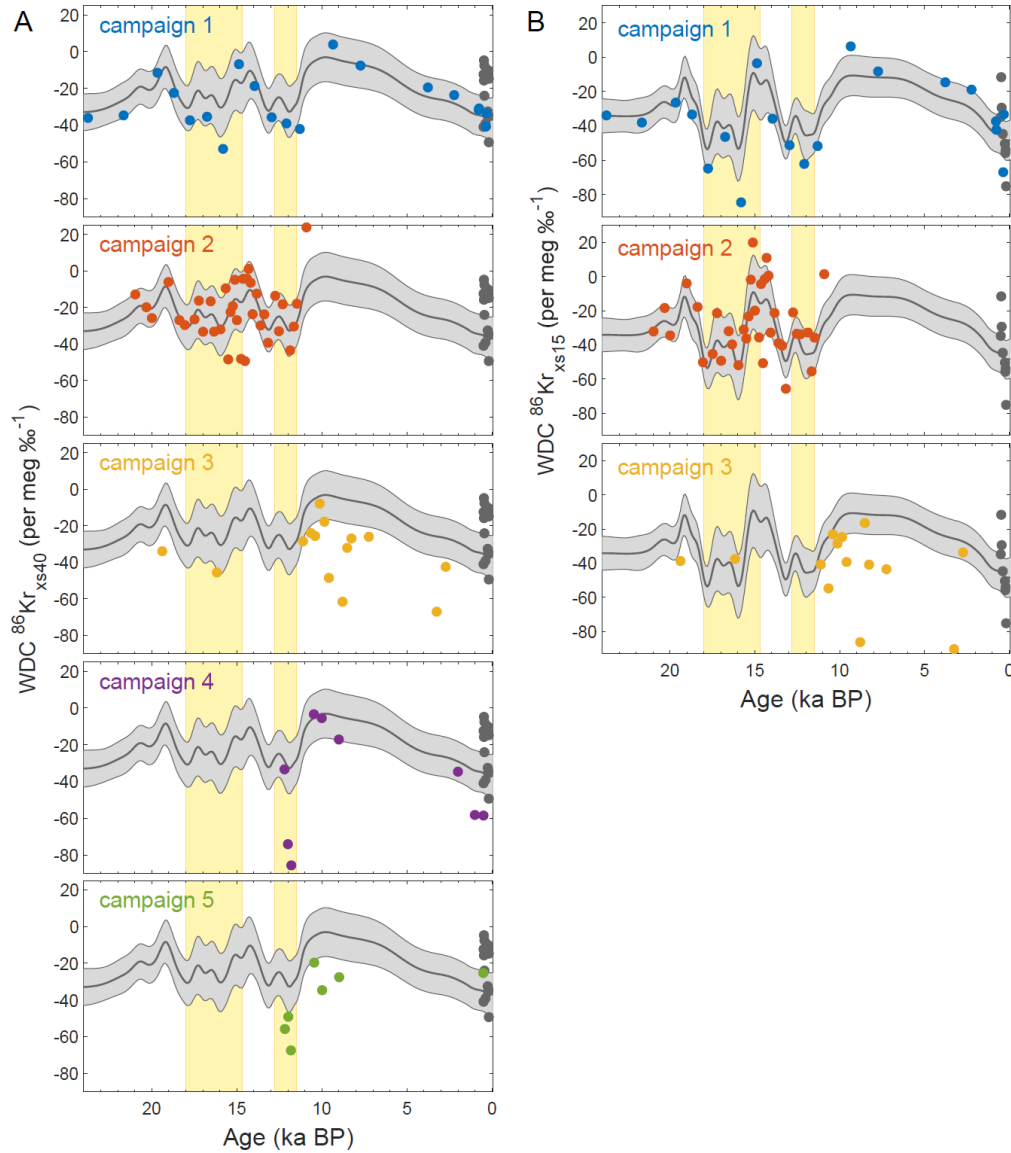
1251

1252 **Figure 4.** Zonal wind speed at 850 hPa (color shading, see scale bar) and 200 hPa (2 m s^{-1} contours)
 1253 regressed onto surface synoptic activity Φ at the Antarctic ice core sites of: **A** WAIS Divide; **B** Law
 1254 Dome (DE08, DE08-OH and DSSW20K); **C** Dome Fuji; **D** James Ross Island. Yellow dots mark the ice core
 1255 locations.



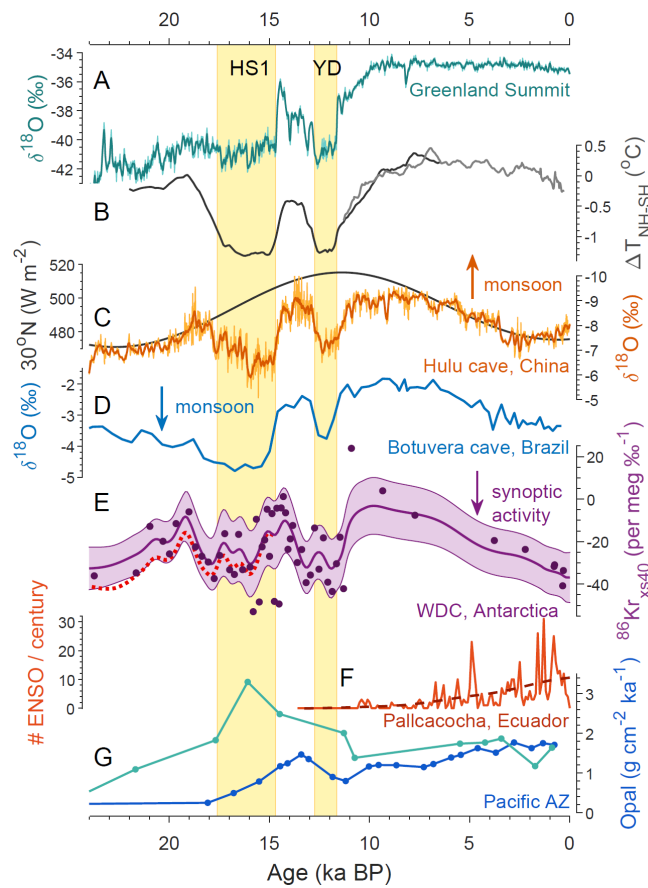
1256

1257 **Figure 5.** Modes of SH extratropical atmospheric variability and their link to synoptic-scale surface
 1258 pressure variability in Antarctica. **A** Annual mean Φ in units of $\% \text{ day}^{-1}$. **B** Colors show correlation between
 1259 Φ and the Southern Annular Mode (SAM) index, with superimposed the 500 hPa geopotential height
 1260 anomalies in 10 m contours (positive contours solid, negative contours dashed). **C** as panel B, but for the
 1261 Pacific-South American Pattern 1 (PSA1). **D** As panel B, but for the Pacific-South American Pattern 2
 1262 (PSA2). SAM, PSA1 and PSA2 are defined as respectively the first, second and third EOFs (Empirical
 1263 Orthogonal Functions) of the 500 hPa geopotential height anomalies in 20° - 90° S monthly values in the
 1264 1979-2017 ERA interim reanalysis (Dee et al., 2011). In all panels the latitude of maximum Φ is denoted
 1265 by the green line.



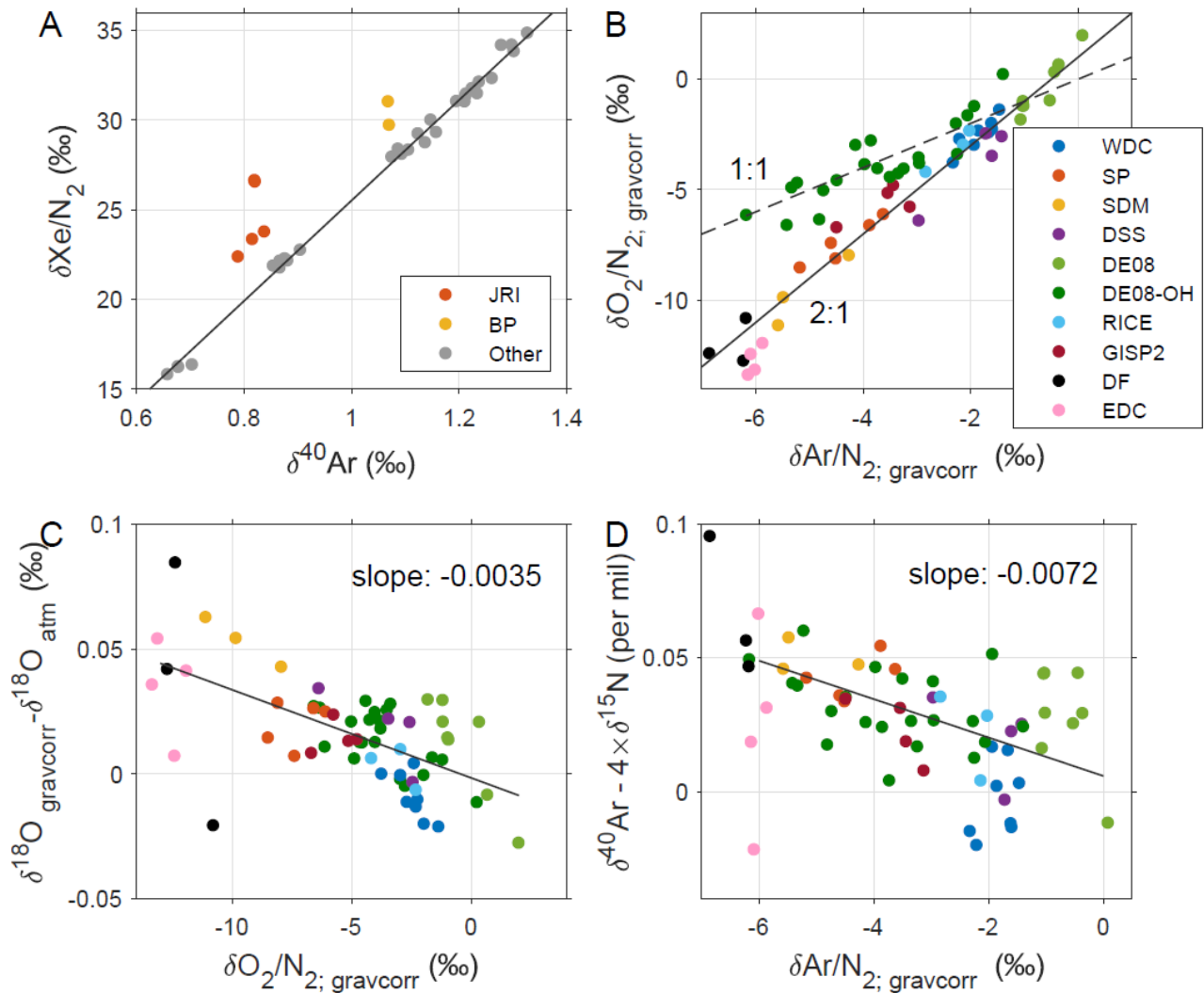
1267

1268 **Figure 6.** WAIS Divide Kr-86 excess records through the last deglaciation. **A** WDC $^{86}\text{Kr}_{\text{xs}40}$ data from the
 1269 five measurement campaigns. The gray curve shows a Gaussian smoothing curve to the combined data
 1270 from the first two campaigns; the light gray shaded area shows the $\pm 1\sigma$ uncertainty envelope based on a
 1271 10,000 iteration Monte-Carlo sampling of the errors and uncertainties. The WDC calibration data is shown
 1272 as gray circles for comparison. **B** As in panel (A), but for $^{86}\text{Kr}_{\text{xs}15}$. For campaigns 4 and 5 the sample was
 1273 not split, and no $\delta^{15}\text{N}$ data are available. The Heinrich Stadial 1 and Younger Dryas North-Atlantic cold
 1274 periods marked in yellow. Thermal corrections in the WDC $^{86}\text{Kr}_{\text{xs}}$ records are based on firm model
 1275 simulations; gas-loss correction is based on a 3rd order polynomial fit to the WDC gravity-corrected $\delta\text{O}_2/\text{N}_2$
 1276 $-\delta\text{Ar}/\text{N}_2$ (Fig. A5).



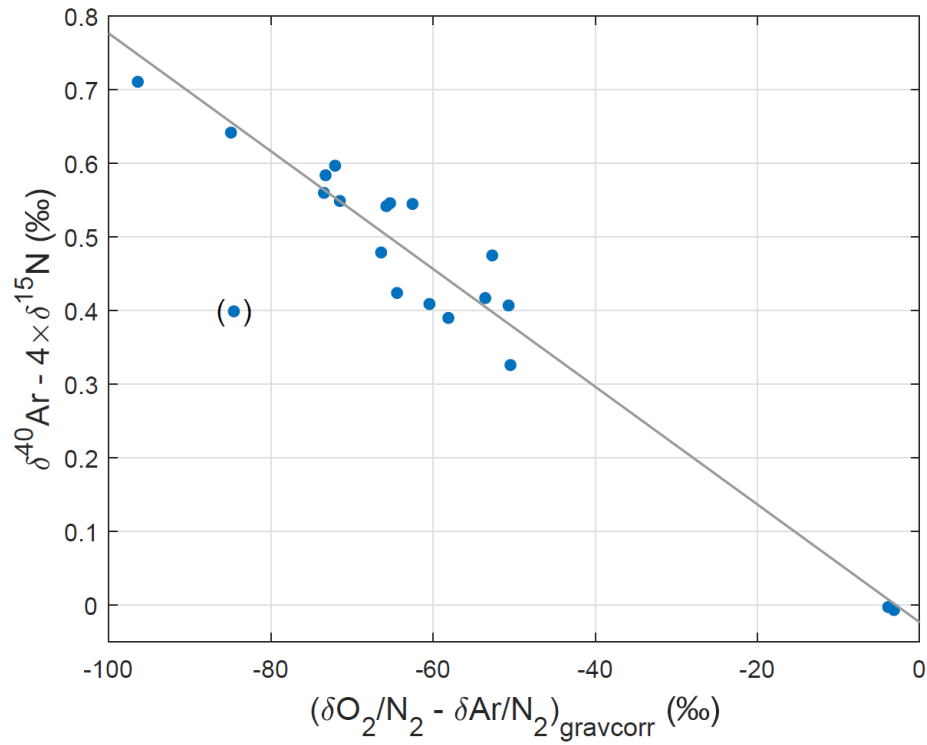
1278

1279 **Figure 7.** Climate records through the last deglaciation with the Heinrich Stadial 1 (HS1) and Younger
 1280 Dryas (YD) North-Atlantic cold periods marked in yellow. **A** Greenland Summit ice core stable water
 1281 isotope ratio $\delta^{18}\text{O}$ here the average of the GISP2 and GRIP ice cores (Grootes et al., 1993). **B** Hemispheric
 1282 temperature difference (McGee et al., 2014) based on global proxy compilations for the Holocene (Marcott
 1283 et al., 2013) and last deglaciation (Shakun et al., 2012). **C** Speleothem calcite $\delta^{18}\text{O}$ from Hulu and Dongge
 1284 Caves, China, as a proxy for East Asian summer monsoon strength (Dykoski et al., 2005; Wang et al.,
 1285 2001). Superimposed is summer solstice (June 21) insolation at 30°N . **D** Speleothem calcite $\delta^{18}\text{O}$ from
 1286 Botuvera cave, southern Brazil, as a proxy for South American summer monsoon strength (Cruz et al.,
 1287 2005; Wang et al., 2007). **E** Kr-86 excess record from WAIS Divide (this study); corrected for gas loss and
 1288 thermal fractionation (Appendix A). Center line and shaded envelope show the mean and $\pm 1\sigma$ uncertainty
 1289 interval of a 10,000 iteration Monte Carlo smoothing exercise (see text). The dotted red line equals the
 1290 center line with a correction for elevation change applied (Appendix A) using a simulated elevation history
 1291 (Golledge et al., 2014). **F** Number of El Niño events per century from laminations in sediments from Laguna
 1292 Pallcacocha, Ecuador (Moy et al., 2002). **G** Th-normalized opal flux in the Pacific Antarctic zone (south of
 1293 the polar front) from cores NBP9802-6PC1 (turquoise; 169.98°W , 61.88°S) and PS75/072-4 (blue;
 1294 151.22°W , 57.56°S), reflecting local productivity and (wind-driven) upwelling (Chase et al., 2003; Studer
 1295 et al., 2015). All isotope data in this figure are on the V-SMOW scale. Arrows show direction of increased
 1296 monsoon strength / synoptic activity.



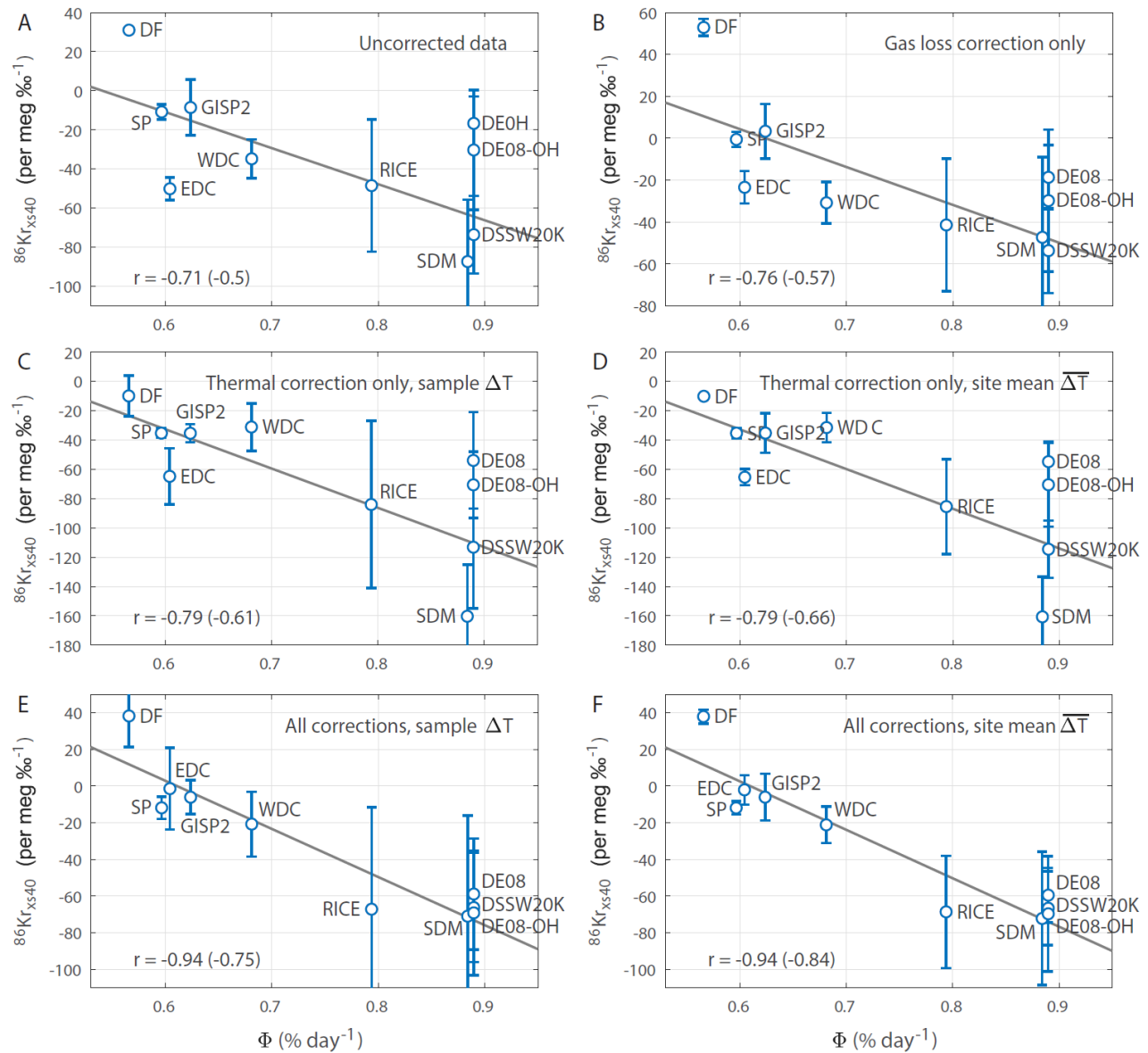
1297

1298 **Figure A1.** Elemental ratios in the 11-site calibration study of late Holocene samples. **A** $\delta\text{Xe}/\text{N}_2$ vs. $\delta^{40}\text{Ar}$
 1299 in all ice core samples. $\delta^{40}\text{Ar}$ is used solely to illustrate gravitational enrichment, and a similar picture arises
 1300 when plotted against any isotopic pair. Refrozen meltwater (elevated $\delta\text{Xe}/\text{N}_2$) was seen in all samples from
 1301 the Antarctic Peninsula (James Ross Island and Bruce Plateau sites), despite selecting samples free of
 1302 visible melt features. **B** The relationship between the commonly used gas loss proxies $\delta\text{O}_2/\text{N}_2$ and $\delta\text{Ar}/\text{N}_2$
 1303 corrected for gravity. **C** Enrichment in $\delta^{18}\text{O}$ (corrected for gravity and atmospheric $\delta^{18}\text{O}_{\text{atm}}$) plotted against
 1304 gravity-corrected $\delta\text{O}_2/\text{N}_2$ **D** $\delta^{40}\text{Ar}$ enrichment plotted against gravity-corrected $\delta\text{Ar}/\text{N}_2$. In all panels
 1305 gravitational correction is applied by subtracting $\delta^{15}\text{N}$ times the atomic mass unit difference.



1306

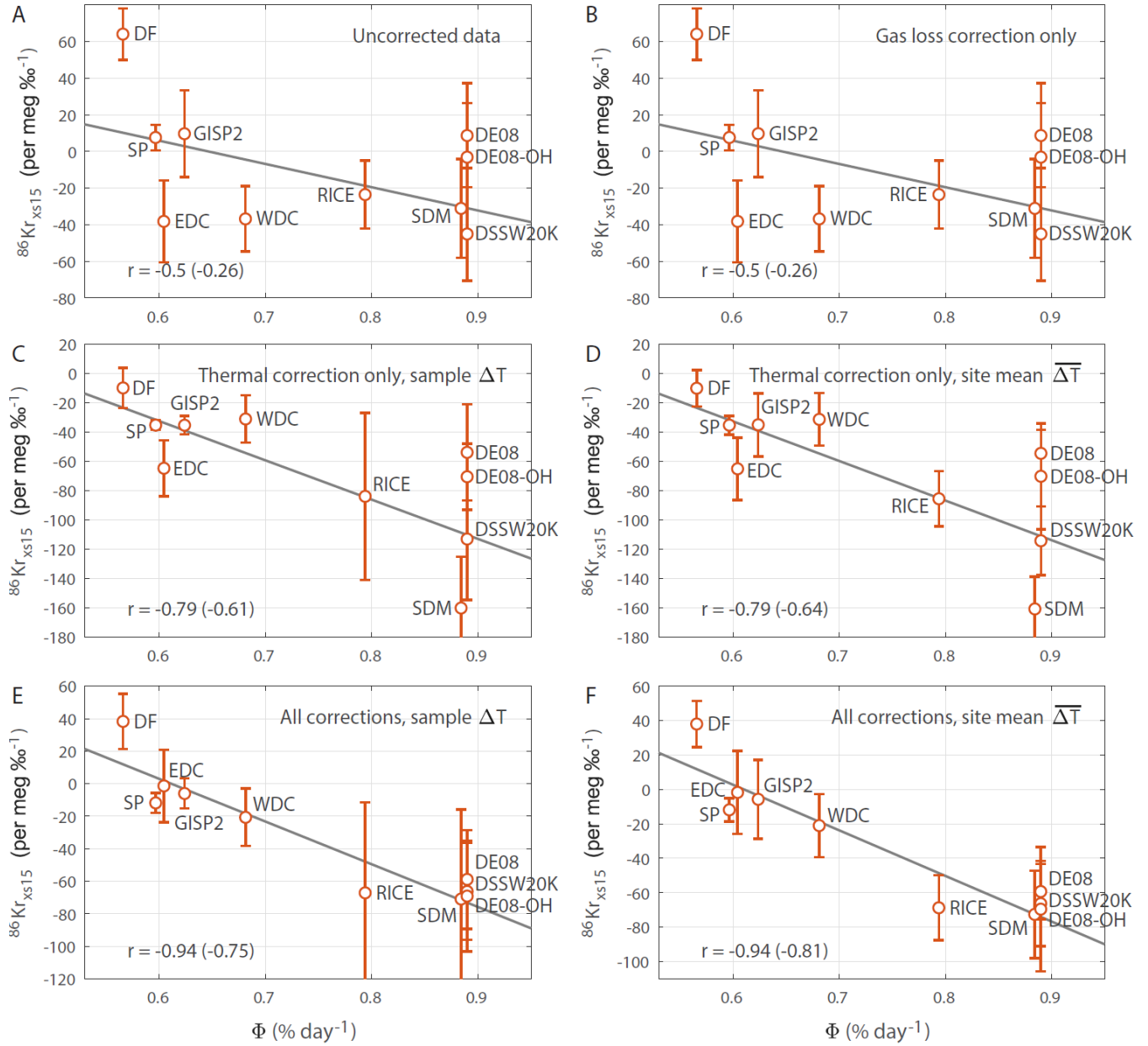
1307 **Figure A2.** Argon isotopic enrichment due to gas loss in the Byrd core used to determine the $\delta^{40}\text{Ar}$ gas loss
 1308 correction (appendix A1). The enrichment in $\delta^{40}\text{Ar}$ plotted as a function of gravitationally corrected $(\delta O_2/N_2$
 1309 $- \delta Ar/N_2)$ measured in the deep Antarctic Byrd ice core, which suffered heavy gas loss. Ice samples were
 1310 analyzed in the Bender Lab at the University of Rhode Island by Jeff Severinghaus in 1997. The slope of
 1311 the least-square fit is $\epsilon_{40} = -0.008$. The data point in parentheses is treated as an outlier and excluded from
 1312 the fitting.



1314

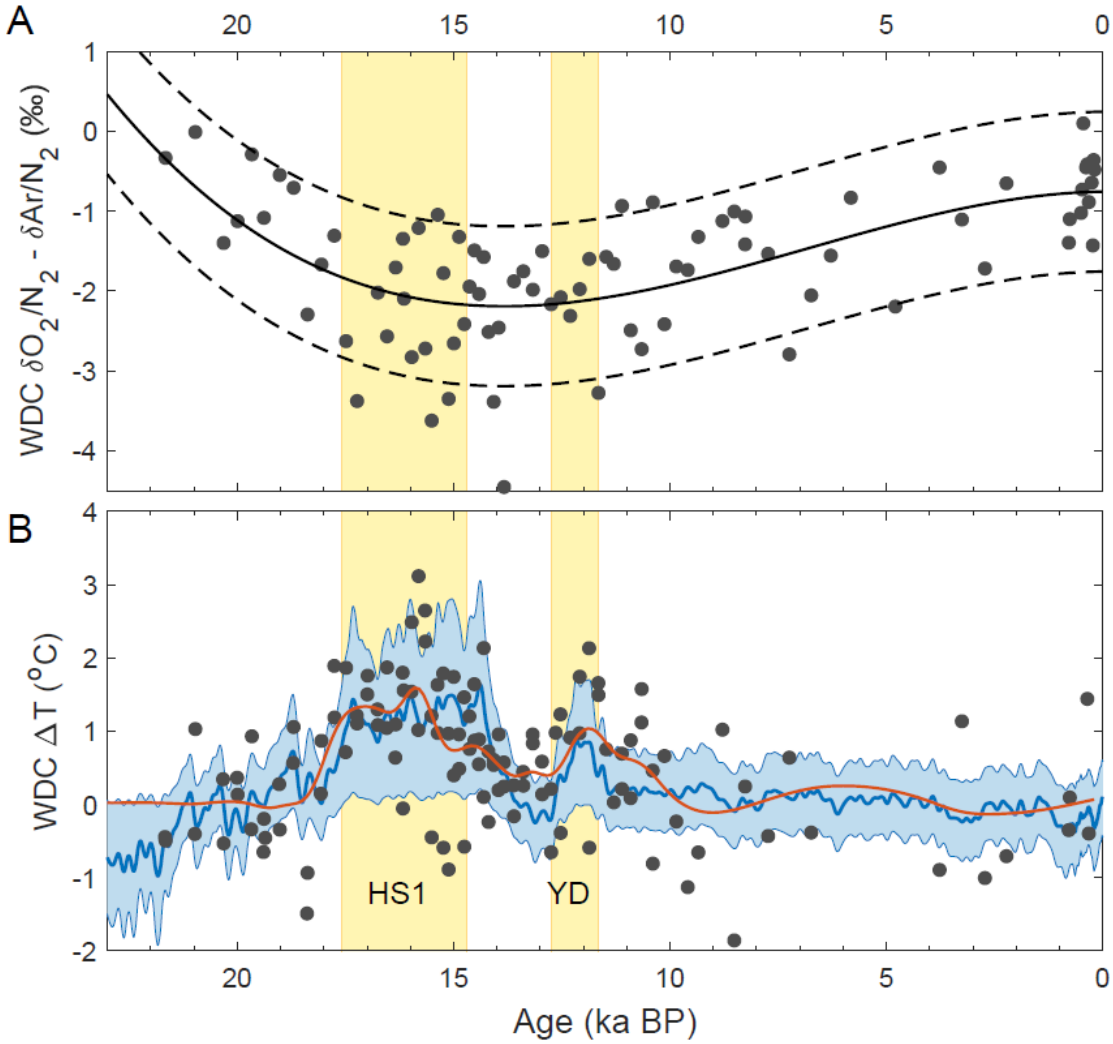
1315

1316 **Figure A3.** Influence of gas loss and thermal correction on the $^{86}\text{Kr}_{\text{xs}40}$ calibration. We plot $^{86}\text{Kr}_{\text{xs}40}$ as a
 1317 function of Φ **A** without any data corrections applied; **B** with only the gas loss correction applied ($\varepsilon_{40} = -$
 1318 0.008); **C** with only the thermal correction applied using individual sample ΔT ; **D** with only the thermal
 1319 correction applied using individual site mean $\overline{\Delta T}$; **E** with both gas loss and thermal corrections applied
 1320 using individual sample ΔT ; **F** with both gas loss and thermal corrections applied using site mean $\overline{\Delta T}$. In
 1321 each panel the correlation to Φ are listed for the site-average and individual sample with the latter in
 1322 parentheses. For all correlations $p < 0.05$.



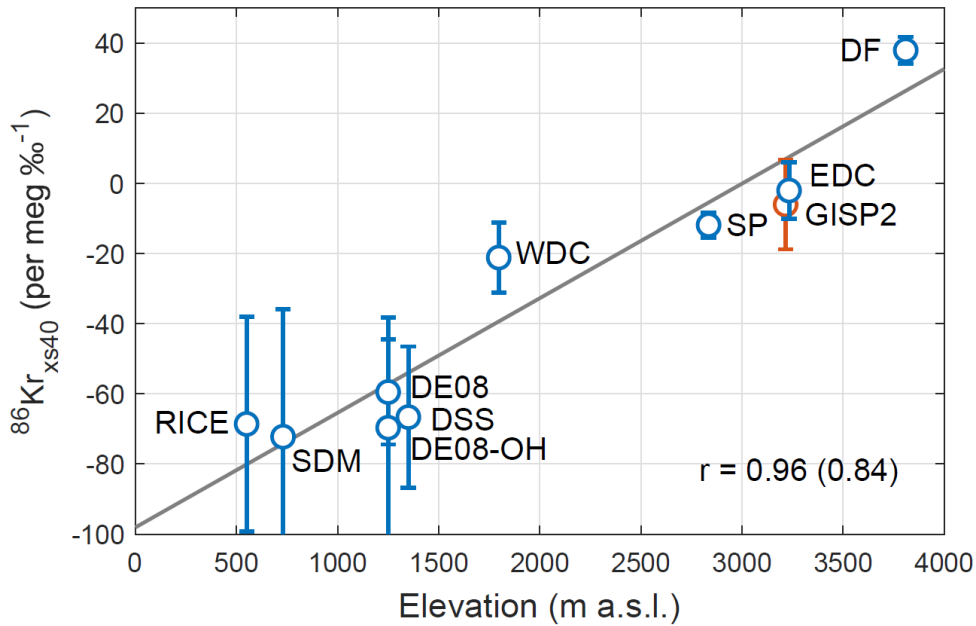
1323

1324 **Figure A4.** Same as figure A3, but for $^{86}\text{Kr}_{\text{xs15}}$. Note that the gas loss correction (panel B) does not impact
 1325 $^{86}\text{Kr}_{\text{xs15}}$. For all correlations $p < 0.05$, except for panels A and B where $p = 0.16$ for the site-average
 1326 correlation.



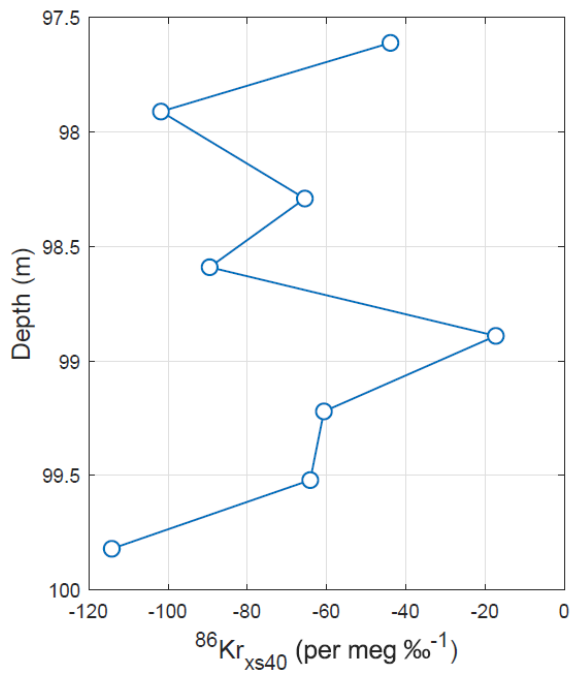
1327

1328 **Figure A5.** Gas loss and thermal corrections for the WDC time series. **A.** WDC gravity-corrected $\delta O_2/N_2$
 1329 $- \delta Ar/N_2$, as a measure of gas loss. The solid line is a third-order polynomial fit to the data; the dashed lines
 1330 give a $\pm 1\%$ range around the fit, which captures the majority of the data. **B.** The ΔT correction applied to
 1331 the downcore records. Blue envelope shows the $\pm 2\sigma$ range of thermal correction scenarios in the Monte
 1332 Carlo sampling, together with the mean (blue line). Gray dots show WDC ΔT estimates from available ^{15}N -
 1333 excess data, with the red curve being a Gaussian smoothing function to the data.



1334

1335 **Figure A6.** Kr-86 excess dependence on site elevation. Vertical axis is the $^{86}\text{Kr}_{\text{xs}}$. The linear fit has a slope
 1336 of 34 per meg ‰^{-1} per 1000 m elevation.



1337

1338 **Figure B1** High-resolution sub-annual sampling of $^{86}\text{Kr}_{\text{xs40}}$ in the DE08-OH site. The annual layer thickness
 1339 at this depth is around 1.3 m.

1340 **Table 1.** Ice core sites used in this study, with N the number of samples included in the calibration study.
 1341 See the main text for acronyms.
 1342

Site	T (°C)	A (m ice a ⁻¹)	Φ (% day ⁻¹)	Latitude	Longitude	N
WDC	-31	0.22	0.68	79.5°S	112.1°W	8 ^a
DF	-57	0.028	0.56	77.3°S	39.7°E	3
SP	-51	0.078	0.6	90.0°S	98.2°W	5
SDM	-25	0.13	0.88	81.7°S	149.1°W	3
DSSW20K	-21	0.16	0.89	66.8°S	112.6°E	4
DE08	-19	1.2	0.89	66.7°S	113.2°E	8
DE08-OH	-19	1.2	0.89	66.7°S	113.2°E	8 ^b
RICE	-24	0.24	0.79	79.4°S	161.7°W	3 ^a
EDC	-55	0.03	0.6	75.1°S	123.4°E	4
JRI	-14	0.68	0.97	64.2°S	57.7°W	5 ^c
BRP	-15	2	0.9	66.1°S	64.1°W	2 ^c
GISP2	-32	0.23	0.62	72.6°N	38.5°W	4

1343 ^a Not including one sample rejected due to technical problems.

1344 ^b Only shallow samples due to strong gas loss in deeper samples attributed to warm storage conditions.

1345 ^c Refrozen meltwater present as indicated by elevated Xe/N₂ ratio.

1346
 1347
 1348
 1349

1350 **Table 2.** Pearson correlation between Φ at the ice coring sites and large-scale atmospheric circulation.
 1351 Correlations are calculated using annual mean data (all months, April-March). We only list the
 1352 statistically significant correlations ($p < 0.1$). The Niño 3.4 is calculated over 5°S - 5°N, 190°E - 240°E,
 1353 using SST from Huang et al. (2014); the PDO index is from Mantua and Hare (2002).
 1354

Site	SAM	PSA1	PSA2	Niño 3.4	PDO	Sea ice Am-Bell	Sea ice Ross
WDC	-	0.31	-	0.31	0.28	-	-
SDM	-	0.47	0.34	0.43	0.45	-	-0.32
RICE	-	0.41	0.34	0.34	0.45	-	-0.30
SP	-	-	-0.32	-	-0.30	-	-
LD	0.45	-	-	-	-	-	-
DF	0.37	-	-	-	-	-	-
EDC	0.30	-	-	-	-	-	-
JRI	0.67	-	-	-	-	0.31	-
BRP	0.68	-	-	-	-	-	-

1355
 1356
 1357